The Quaternary monogenetic Bayuda Volcanic Field, Sudan – Insights into mantle and crustal processes during magma petrogenesis

Francois J.P. Lötter[a], Nils Lenhardt[a,*], Lothar Viereck[b], Carsten Münker[c], Chris S. Marien[c], Mohammed A.H. Altigani[d]

[a]University of Pretoria, Department of Geology, Private Bag X20, 0028 Pretoria, South Africa
[b]Friedrich-Schiller-Universität Jena, Institut für Geowissenschaften, Burgweg 11, 07749 Jena, Germany
[c]Universität zu Köln, Institut für Geologie und Mineralogie, Zülpicher Str. 49b, 50674 Cologne, Germany
[d]Al Neelain University, Department of Mineral Wealth, P.O. Box 12702, 11121 Khartoum, Sudan

*Corresponding author: Department of Geology, University of Pretoria, Private Bag X20, 0028, Pretoria, South Africa. Email: nils.lenhardt@up.ac.za

Highlights

- First reconstruction of the petrogenesis in the Bayuda monogenetic volcanic field.
- BMVF is a sodic-alkaline volcanic field with OIB signature.
- BMVF magmas originate from mixing of a prevalent mantle with a HIMU-like component.
- Most rocks formed from amphibole-garnet lherzolitic source and < 10% partial melting.

Abstract

The Holocene Bayuda Monogenetic Volcanic Field (BMVF) is located at the Great Bend of the river Nile in the north of Sudan. The analysed volcanic rocks are of basanitic to hawaiitic composition, characterising the BMVF as a sodic-alkaline volcanic field. Petrographic evidence documents olivine and clinopyroxene as the main fractionating phases as well as FC processes that were accompanied by assimilation of mantle and crustal rocks in addition to mingling and mixing processes. Utilising systematic differences in trace element variations, two primary magmas of Series A and B can be distinguished. Uniform normalised incompatible element patterns, e.g. LREE enrichment accompanied by HREE depletion, negative anomalies of K and Pb, and modelling based on partition coefficients of La, Dy and Yb in mantle residues, suggest partial melting of an amphibole-garnet lherzolite. The presence of amphibole provides a constraint, implying that the melt was derived from a metasomatised lithospheric mantle. The presence of the Pb-depletion (documented by Ce/Pb ratios of >30) suggests that all magmas are of HIMU-OIB type. This is supported by their uniform $^{87}Sr/^{86}Sr$ (0.703010–0.703347), $^{143}Nd/^{144}Nd$ (0.512869–0.512995), $^{206}Pb/^{204}Pb$ (19.787–19.895), $^{207}Pb/^{204}Pb$ (15.656–15.653) and $^{208}Pb/^{204}Pb$ (39.560–39.678) isotope characteristics. Additionally, we can describe the HIMU character of the NE African mantle with respect to $^{176}Hf/^{177}Hf$ (0.283006–0.283026). The mantle source of the BMVF magmas appears to have the composition of the common mantle "C" with an overprint by a HIMU component, resulting in higher radiogenic $^{206}Pb/^{204}Pb$ ratios above 19.5 (FOZO-HIMU-OIB type). We attribute this to the metasomatic character of the lithospheric mantle. The Hf/Nd isotope characteristics of the BMVF suggest that this metasomatism in the mantle source is most probably late Pan-African in age. When compared to circum-Mediterranean and regional volcanic fields, the

high radiogenic Pb character of the BMVF indicates that their genesis cannot be related to magmatism associated with the activity of the Afar plume event and consequential magmatism along the Main Ethiopian Rift and the Red Sea Rift, as they are all of low radiogenic character.

Keywords: Bayuda Volcanic Field; African volcanism; Intraplate volcanism; HIMU-signature; Mantle metasomatism

1. Introduction

So far, the large polygenetic volcanoes along the major rift zones of Cameroon and the Afar rift system have been the predominant focal point of studies on Cenozoic volcanism in Northern Africa. Within the anorogenic alkaline volcanic fields, distributed away from major rift zones, the edifices of polygenetic volcanoes garner more attention than monogenetic volcanoes that have been basking in the shadow of their larger counterparts (e.g., Mount Cameroon; Ngwa et al., 2019).

Németh and Kereszturi (2015) defined a monogenetic volcano as "a volcanic edifice with a small cumulative volume (typically ≤1 km^3) that has been built up by one continuous, or many discontinuous, small eruptions [that] occurred in a short timescale (typically ≤10 of years) and [were] fed from one or multiple magma batches through a relatively simple, closely spaced feeder dyke (and sill) system with no associated well-developed magma chambers." Monogenetic volcanic fields may be built up by as many as several hundred monogenetic volcanoes (scoria cones, tuff rings, maar volcanoes) and, contrary to a single monogenetic volcano, may have lifespans of up to millions of years (Wijbrans et al., 2007), comparable to that of a polygenetic stratovolcano (Németh, 2010). The plumbing system of a monogenetic volcanic field can be immensely complex and can have a significant influence on the form and composition of different eruptions within a single volcano (Brenna et al., 2011). The same authors inferred through geochemical analysis on the stratigraphy of several monogenetic volcanoes that eruptions differing only by days may also differ geochemically.

While Cenozoic monogenetic fields of mafic alkaline magmatism are rare in the rest of Africa, e.g. the Tombel Graben monogenetic volcanic field in western Cameroon (Nkouathio et al., 2002) and the Lake Natron-Engaruka monogenetic volcanic field in Tanzania (Dawson, 2008), they are widespread throughout North Africa from the Canary Islands in the west to Sudan in the east (Kereszturi et al., 2013; Liégeois et al., 2005; Lucassen et al., 2008).

The Bayuda desert province in the north of Sudan contains five Cenozoic volcanic fields (Almond et al., 1984) (Fig. 1B): the Northern Field, the south-eastern Abu Rugheiwa Field (named Jebel Umm Arafieb in Lucassen et al., 2008), the Shaq Umm Bosh Field and the Wadi Muqaddam Field in the southwest (combined to the Gebel Kurbei Field in Lucassen et al., 2008) as well as the Bayuda Monogenetic Volcanic Field (BMVF) in the northwest (named Bayuda Main Volcanic Field in Lucassen et al., 2008).

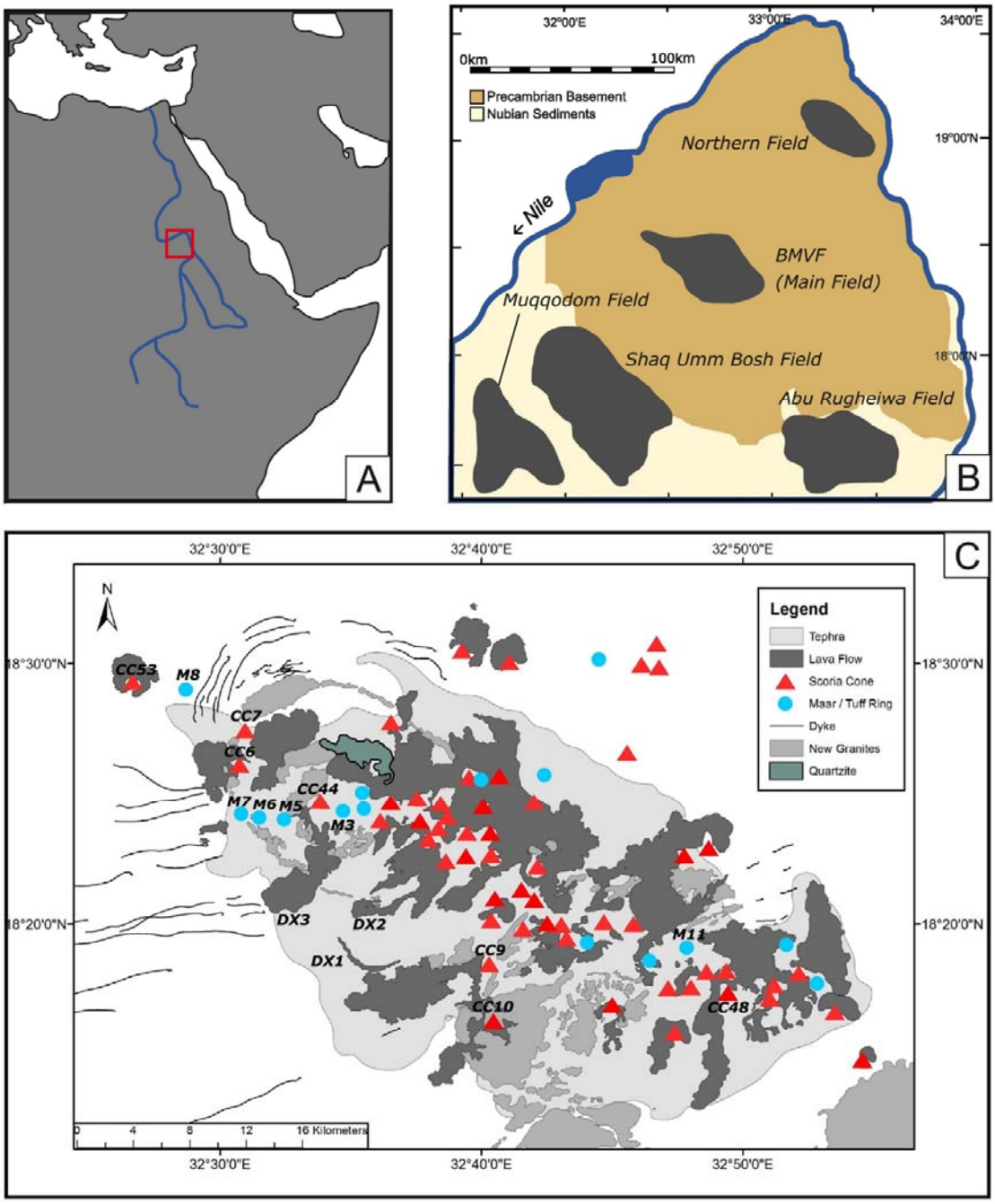

Fig. 1. A) Location of the Bayuda Desert. B) Distribution of volcanic fields inside the Bayuda Desert (modified from Almond et al., 1984). C) Simplified geological map of the BMVF showing the different types of volcanoes and sample locations in the field (modified from Almond et al., 1969).

The BMVF is a relatively poorly studied volcanic field that still lacks comprehensive geochemical analysis and detailed age dating (Almond, 1974; Almond et al., 1984). Lucassen et al. (2008) were the first to present Nd-, Sr- and Pb-isotope data for several Cretaceous to Quaternary volcanic fields in Sudan and southern Egypt to derive a conceptual model for the evolution of the lithospheric mantle beneath NE Africa. Lenhardt et al. (2018) described the volcanology of maar deposits and scoria cones in the BMVF in detail. This contribution sets

out to derive a petrogenetic model and to constrain the evolution of the magmas based on petrography and geochemical (major, trace elements as well as Nd-, Sr-, Pb- and Hf-isotopes) analyses of unweathered lava and tephra samples of the BMVF. In addition, the mantle source of the BMVF is estimated by comparing the isotopic signature of samples from volcanic fields in North Africa, East Africa, Arabia, and Central Europe.

2. Geological setting

The Bayuda Desert is located in and around the Great Bend of the Nile in the Sudan. Its basement is made up of three terranes: The Bayuda terrane forms the largest section of the desert and is separated by the Atmur-Delgo suture from the Gabgaba terrane in the east and by the Keraf suture from the Halfa terrane in the north (Abdelsalam et al., 2003; Lenhardt et al., 2018) (Fig. 1B). The Keraf suture also separates the Archean Sahara Metacraton from the Neoproterozoic Arabian Nubian-Shield (ANS) (Liégeois et al., 2013).

The rocks of the Bayuda Desert basement are of Neoproterozoic age and predominantly consist of medium-grade gneisses and high-grade migmatites with volcaniclastic rocks, separated by occasional ophiolites (Barth and Meinhold, 1979). Approximately 25 different alkaline ring complexes are hosted along WNW-ESE to NW-SE striking lineaments within the Bayuda Desert basement (Vail, 1985). These ring complexes formed during different magmatic phases that occurred between 460 and 159 Ma independent of orogenic deformation in an intraplate environment (Vail, 1985). The ring dykes formed between A-type granite plutons where they spatially overlap with each other. Early phases of these ring complexes were volcanic with sequences of trachytic lava flows and ignimbrites outcropping in collapsed calderas (Vail, 1985). The plutonic phases of the ring complexes are highly alkaline, consisting of alkali granite and alkali syenite (Vail, 1985). These ring dykes are compositionally similar to a collection of dykes striking E-W in the desert. The dyke swarms and ring dykes, alongside the A-type granitic plutons, are younger than the gneissic basement and are referred to as the Young Granites (Almond et al., 1969).

Within the Bayuda Desert several volcanic fields developed (Almond et al., 1984) (Fig. 1B) for which a late Cretaceous to Pleistocene (70–0.9 Ma) volcanic activity is indicated by K-Ar dating (Almond et al., 1984; Barth and Meinhold, 1979).

The BMVF is NW-striking and appears to be located between two major lineaments of ring complexes, overlying a minor cluster of ring complexes, called the New Granites in Fig. 1C. The BMVF represents the youngest of the volcanic fields in the Bayuda Desert, consisting of a well-preserved group of volcanoes that seem to have experienced most eruptions during the Pleistocene (1.7–0.9 Ma) (Barth and Meinhold, 1979). The most recent eruption (1102 ± 48 B.P.) was indirectly determined through ^{14}C-dating of a baked piece of mammalian dung, preserved on one of the volcano's edifices (Vail, 1988). The preservation of the cones is attributed to this recent formation of the volcanic field and the arid weather of the Bayuda Desert.

Based on the observations of Lenhardt et al. (2018), the majority of the ca. 70 monogenetic volcanoes within the BMVF are cinder cones, except for 15 maar volcanoes and tuff rings that are concentrated in the south and the north of the field (Fig. 1C). Lenhardt et al. (2018)

showed that at least one cinder cone (Bayt al-nur) in the BMVF experienced a phreatomagmatic phase that followed an initial purely magmatic phase.

Most of the cinder cones show signs of erosion due to breaching. Sub-circular lava fields slope gently away from the breached cones. Most of the flows can be described as ʻaʻā lava. Pāhoehoe lava flows were only seen as intercalations between layers of pyroclastic fallout that formed during the early stages of cinder cone formation, probably due to rootless lava flow formation from spatter fall.

The vast lava flow units of the BMVF reach thicknesses of up to 30 m and exhibit a massive, sometimes columnar jointed central part and a blocky, highly vesicular carapace. The hummocky flows are covered by rounded to spinose hillocks and narrow, steep-sided ridges, which are often aligned in the flow direction. These various prominences are mostly less than 5 m high but exceptionally reach 10 m in height. Some appear to be pressure ridges but most are tumuli or blisters, which, when observed in section, are seen to consist of an outer layer of stretched, scoriaceous lava full of flattened vesicles, an inner layer of more massive lava, and an altered rubbly core (cf. Almond et al., 1969). According to Almond et al. (1969), a scattering of spindle-shaped bombs among the scoriaceous blocks mantling the surface of the flows suggests that some of the tumuli developed into spatter cones.

Almond et al. (1984) reason that the BMVF formed in an arid environment, but Lenhardt et al. (2018) argue that the evidence of phreatomagmatic eruptions implies that the BMVF formed during wetter conditions, for instance, during the time of 9000–6000 BP when the Bayuda Desert experienced a time of higher rainfall and higher groundwater tables.

3. Materials and methods

Sample collection was mostly restricted to the western side of the BMVF as it is more accessible than the rest of the field (see Table 1 in Appendix A for coordinates). In total, 44 samples were collected from nine lava flows, the edifices of five maar volcanoes, one tuff ring, and one cinder cone. Petrographic thin sections were made from all samples.

Nine thin sections from seven volcanoes and one lava flow were selected for electron microprobe analysis and a total of 70 olivines, 14 clinopyroxenes and 8 plagioclases (phenocrysts and microcrysts) were analysed. The measurements (quantifying the elements Na, Mg, Si, K, Ca, Ti, Fe, Mn, Cr, Ni, and Al) were taken at the centre ("core") and close to the edge ("rim") of the crystal taking care to avoid accidental groundmass measurements. The analyses were carried out on a CAMECA SX 100 electron microprobe at the University of Johannesburg. An acceleration voltage of 20 kV and a current of 20 nA were used for quantitative spot analysis. Point measurements were set to 200 seconds measuring time.

After milling in a tungsten-carbide milling pot, major element and selected trace element analyses of all the samples were carried out using a Thermo Fischer ARL Perform ʻX Sequential XRF instrument with OXSAS software at the University of Pretoria. SARM 49 was used for quality control. Forty-four samples were selected for XRD analyses and 12 samples were selected for XRF analyses. The XRD samples were analysed using a PANalytical Aeris powder diffractometer with a PIXcel detector and fixed divergence- and receiving slits with Fe filtered

Co-Kα radiation (λ = 1.789 Å). The phases were identified using X'Pert Highscore plus software. The relative phase amounts (weight%) were estimated using the Rietveld method employing the X'Pert Highscore plus software.

ICP-MS trace element analyses of all the samples were completed at the University of Witwatersrand (WITS) and the University of Cape Town (UCT). Trace element analyses performed at UCT used an Xseries2 Thermo Fischer machine with Argon as the carrier gas at 10 ms dwell time. The calibration curves were determined by using artificial, multi-element standards. A detailed description of the procedure can be found in Harris et al. (2018). Trace element analyses at WITS were performed on an ELAN DRC-e ICP-MS, manufactured by PerkinElmer Sciex. Samples were analysed in conjunction with BCR-1, BHVO-1, and BIR-1 control standards. A detailed description of the procedure can be found in Vonopartis et al. (2020).

Isotope analysis was performed on selected samples. Ten samples were selected for Hf, Nd, and Sr isotope analysis and six for Pb isotope analysis due to limited sample quantity. A blank and a certified BHVO-2 standard were used for quality control (Govindaraju, 1994). The samples that were selected for Hf, Nd, Sr, and Pb isotope analysis were nine basanites and one trachybasalt that were free of secondary alteration, amygdales, and xenoliths. All 10 samples were pulverised in an agate mill. The chemical separation for Hf-Nd-Sr was performed on ca. 120 mg of powder for each sample that was cleaned with 6 N HCl to remove carbonates and secondary zeolites. Subsequently, the samples were digested in a 1:1 mixture of 14 M HNO_3 / 24 M HF for 24 h at 120°C. After fuming down, 14 M nitric acid was repetitively added to remove possible fluorides from the solution. Hafnium was separated from the matrix following the procedure by Münker et al. (2001). Strontium and Nd were obtained from the residual matrix of the Hf-separation by using BioRad AG50W-X8 cation resin (200–400 mesh) and Ln-Spec resin following Pin and Zalduegui (1997). Eluted Pb cuts were obtained from six ~200 mg of 2–4 mm sized whole-rock chips. After subsequent cleaning with 2.5 N and 6 N HCl for 1 h, the samples were digested and Pb was eluted after the description of Kirchenbaur et al. (2012). The blank sample was cross-contaminated during Sr-isotope measurement by ~200 ppb of contaminant, which is negligible due to the high Sr contents of the measured samples. The Sr, Nd, Hf, and Pb isotope measurements were achieved through isotope dilution on the Thermo-Finnigan Neptune MC-ICP-MS at the University of Cologne, Germany. Nd isotope ratios were corrected for mass fractionation to $^{146}Nd/^{144}Nd = 0.7219$ and reported results are given relative to the La Jolla $^{143}Nd/^{144}Nd$ of 0.511859. $^{176}Hf/^{177}Hf$ concentrations were normalised to a $^{179}Hf/^{177}Hf$ ratio of 0.7325 and reported results are given relative to the $^{176}Hf/^{177}Hf = 0.282160$ of the Münster AMES standard that is indistinguishable from JMC 475 (Blichert-Toft et al., 1997). Strontium isotopes were normalised to $^{86}Sr/^{88}Sr = 0.1194$ and are given relative to $^{87}Sr/^{86}Sr$ of 0.71024 for NBS 987. Lead isotopes were measured and normalised to the doped NBS 997 Tl standard and are relative to NBS 981 with $^{206}Pb/^{204}Pb = 16.9405$, $^{207}Pb/^{204}Pb = 15.4963$, and $^{208}Pb/^{204}Pb = 36.7219$ (Galer and Abouchami, 1998). Procedural blanks were typically <70 pg Hf and Nd, and < 25 pg Pb. Only the procedural blank for Sr yielded 7.4 ng. The external long-term reproducibility is ±40 ppm for Hf and Nd, ±50 ppm for Sr, and ± 130 ppm for the Pb isotopes (2 RSD).

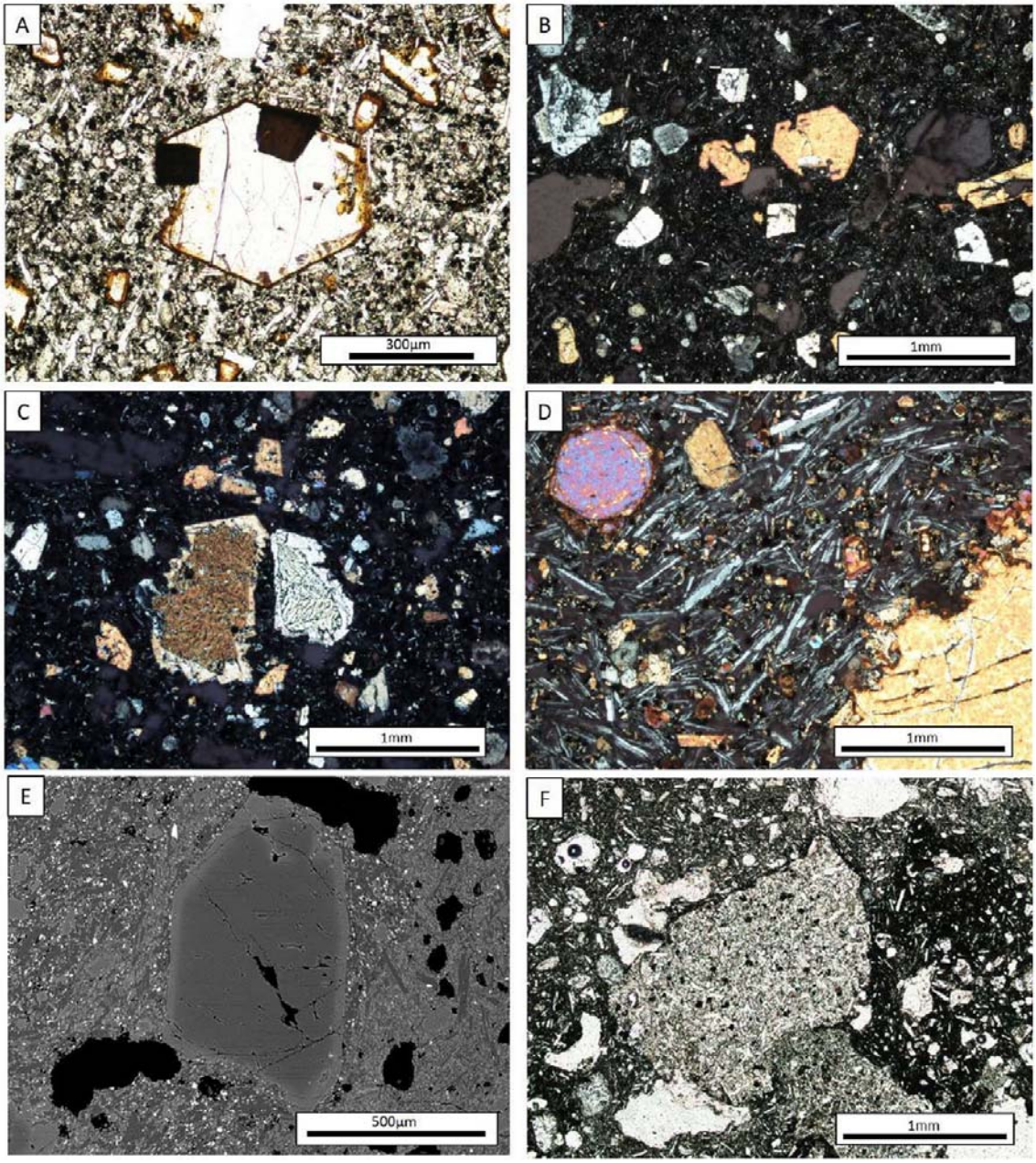

Fig. 2. Micrographs of the general mineral assemblages of the BMVF. A) Olivine phenocryst with spinel inclusions, plane polarised light (DX3, sample B11). B) Skeletal texture of olivine phenocrysts, cross polarised light (CC9, sample B07). C) Pronounced sieve textures in clinopyroxene phenocrysts, cross polarised light (CC10, sample B04). D) Lava flow displaying trachytic texture with olive and clinopyroxene phenocrysts, cross polarised light (M11, sample V-1). E) Electron Backscatter Image of a mantled olivine in a matrix displaying different degrees of crystallinity (CC48, sample II-2). F) Electron Backscatter Image of a co-magmatic xenocryst hosted in a matrix displaying different degrees of crystallinity, plane polarised light (CC44, sample B12).

4. Results

4.1. Petrography

The volcanic rocks of the BMVF consist of vesicular, mafic lava flows (DX), and tephra deposits of cinder cones (CC) and maars or tephra rings (M). The lavas and tephra predominantly display porphyritic textures, occasionally with glomerocrysts. Phenocrysts (>300 μm) make up ~30% of the lavas and tephra deposits, consisting of 15% olivine, 15% clinopyroxene, and <0.5% brown spinels of the chromite series. Olivine phenocrysts have a subhedral to euhedral crystal habit (~0.3–4.8 mm in size). Clinopyroxenes are subhedral-euhedral and often occur as broken crystals (~0.3–4.5 mm in size). Melt inclusions are rare.

The clinopyroxenes exhibit normal to anomalous interference colours. They are characterised by oscillatory zoning with increasingly darker brown interference colours outwards. This directed zoning is often interrupted in larger phenocrysts by one or repetitive internal anhedral boundaries of changes in interference colours. Both olivine and clinopyroxene phenocrysts show dissolution textures such as embayments and skeletal morphology (Fig. 2B and C). Clinopyroxenes commonly display anhedral, often green coloured or sieve textured cores with mantle overgrowths, frequently with serrated outer rims (Fig. 2C). Unmantled clinopyroxenes with anhedral sieve textures occur very rarely (CC10, samples B05 and V03; CC 44, sample B12). Inclusions of spinels of the chromite series are usually hosted in olivine and less often in clinopyroxene phenocrysts (Fig. 2A). Individual spinel phenocrysts are rare and typically rimmed by an opaque spinel of the magnetite series.

The basanite's groundmass textures vary from intergranular (lava flows and lithic co-magmatic xenoliths) to various types of intersertal. Furthermore, the groundmass exhibits microcrysts (<300 μm) of plagioclase laths, almost tetragonal (with (010) faces being suppressed) olivine, slightly elongated clinopyroxene with anomalous birefringence and sector zoning, as well as cubes of oxides. In the intergranular matrix of lava flows we can identify (1) a bimodal distribution of oxides (~10 μm and ~30 μm) and (2) isometric crystals of nepheline (DX1) (presence supported by XRD). While the groundmass of the hawaiite M11 (Fig. 2D) (cf. section 4.3.1, Fig. 6) qualitatively shares the same minerals as that of the basanites, it is richer in plagioclase and displays an initial trachytic texture. We identified apatite neither in the matrix of basanites nor hawaiites. However, minor element variations require apatite as fractionating solidus phase (see section 5.1).

The matrix does not always appear uniform throughout the samples from volcanoes M6, CC10, CC44 and CC48. Within individual thin sections, matrices of different crystallinity can be differentiated by (1) the amount of tachylitic matrix (Fig. 2F), (2) the size and variable length-width ratios of plagioclase crystals (Fig. 2E), and (3) the amount of oxides (Figs. 2E).

Xenocrysts are present within thin sections of individual lava flows and tephra samples as (1) resorbed orthopyroxenes, exhibiting exsolution lamellae and oxide staining (DX 1, sample B08), (2) resorbed orthopyroxenes, jacketed by clinopyroxene and grading from a columnar to vermicular morphology (CC44, sample B12), (3) resorbed orthopyroxenes of clinoenstatite composition (magnesium number (Mg# 62), partly replaced by clinopyroxene (Mg# 71) (CC48, sample II-2), (4) lherzolitic Cr-diopside (Mg# 86, Cr_2O_3 = 1 wt%), mantled by clinopyroxene

(Mg# 72) (CC10, sample V01), (5) resorbed colourless garnet, kelyphite-rimmed (CC44, sample B12), (6) resorbed, emerald green coloured uvarovitic garnet or spinel of the Al-spinel series with oxide rims (M6, sample B20), (7) subhedral brown, oxide-rimmed mica (CC48, sample II-2), (8) resorbed plagioclase without reaction rim that has been fractured along the cleavage on (001) (CC44, sample B12, and CC48, sample II-2), and (9) resorbed quartz without a reaction rim in a sample from maar tephra (M8, sample V07).

Xenoliths are rare in the samples we selected for this study but occur as (1) almost completely assimilated leucocratic rock, the rest of which shows a tear-like form and is rich in green needles, most likely Na–Fe pyroxenes (DX1, sample B08), and (2) co-magmatic intergranular basanitic fragments (CC44, sample B12; Fig. 3E). However, field observations indicate manifold assemblages of crustal and mantle xenoliths (Lenhardt et al., 2018; Lucassen et al., 2011).

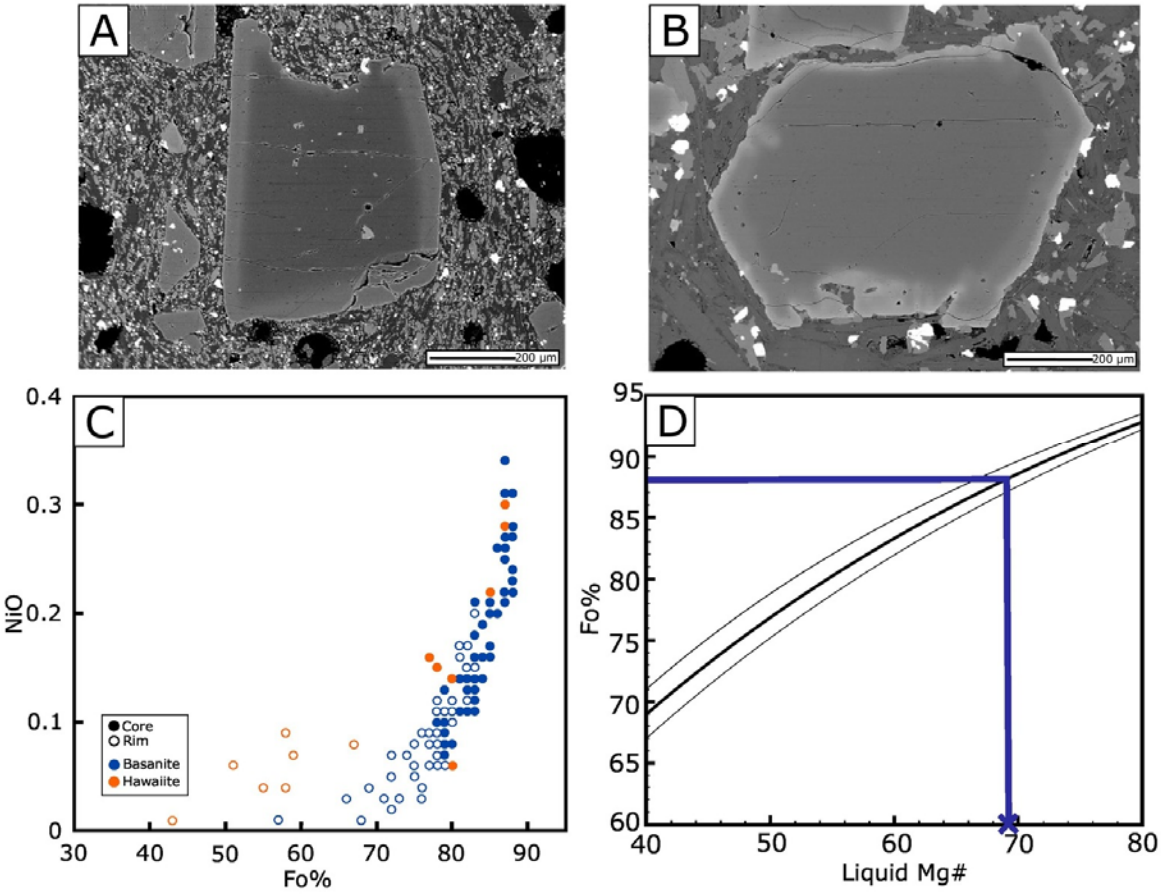

Fig. 3. A) Electron Backscatter Image of a basanite-hosted dark, euhedral olivine core with pronounced, lighter mantle. B) Electron Backscatter Image of a hawaiite-hosted olivine, displaying two mantles of lighter colour around a dark euhedral core. C) NiO vs. Fo% diagram, displaying the cores and rims of olivine phenocrysts hosted in basanites and the hawaiite. D) Fo% vs. Liquid Mg# diagram, showing the Mg# of the melt in which the olivine with the largest Fo% crystallised (see text for reference).

Despite the lavas' vesicular textures, amygdales are uncommon within the lava flows and tephra deposits. However, if present, they contain either one or two phases of secondary

minerals, predominantly a carbonate phase and a subordinate zeolite phase of the chabazite group (identified by XRD). In samples from eruption centres CC6, CC9, CC10, M6, M7 and M11, carbonate additionally occurs as an interstitial phase.

4.2. Single mineral chemistry

Chemical compositions were determined for selected olivines, clinopyroxenes and plagioclase by EMP analyses.

4.2.1. Olivines

The analysed olivine phenocrysts range in composition from Fo% 88 to Fo% 42. Backscatter images (Figs. 3A and B) show wide cores that are mantled by narrow rims. Within the phenocrysts of the hawaiite (M11), we can distinguish between an inner and an outer rim (Fig. 3B). Documenting the mineral analyses, we distinguish between core and rim compositions (Fig. 3C). Olivine cores in basanites only show a small variation in Fo% 88–78 that is accompanied by a large variation in NiO contents from 0.35–0.07 wt%. The associated rims range from Fo% 81–57 while NiO contents range from 0.2–0.01 wt%. The olivine cores in the hawaiite sample from M11 (Fig. 3B) range from Fo% 86–76 with NiO contents of 0.3–0.06 wt%. The compositions of the rims vary from Fo% 68–43, NiO contents from 0.95–0.01 wt%. Thus, while the cores in the basanites and the hawaiite almost cover the same range in compositions, the rims in the hawaiite are lower by about Fo% 14 at identical NiO contents. Using the method of Roeder and Emslie (1970), based on the highest Fo% of 88, we calculated the Mg# of the parental melt of the basanites and the hawaiite as 69–70 (Fig. 3D).

4.2.2. Clinopyroxenes

The analysed pyroxenes are mainly Ca-rich clinopyroxenes (Fig. 4) (see Appendix A, Table 3). The petrographic observations show that the pyroxene phenocrysts are zoned and exhibit cores and rims, which were measured separately (Fig. 4). The composition of the rims varies only slightly from $Mg_{40}Fe_{12}Ca_{48}$ to $Mg_{32}Fe_{15}Ca_{53}$. In contrast, the cores cover a wide range from $Mg_{41}Fe_{10}$ to $Mg_{22}Fe_{29}$ at an almost constant *Wo* content of ~49 ±2. Therefore, further on, descriptions of the observed zonations will be based on the Mg#. In phenocrysts with anomalous interference colours, oscillatory zoning is exhibited with overall normal zoning outwards from Mg# 78–74 to 72–67. With decreasing Mg#, CaO and Na_2O vary between 21 and 23 wt% and 0.4–1.9 wt%, respectively. Cr_2O_3 correlates positively with Mg#, decreasing from 0.44 wt% to less than 0.1 wt%. In contrast, TiO_2 correlates positively with Ca, increasing from 1 to 2.5 wt% to values larger than 4 wt% (max. 6 wt%) at Mg# smaller than 70 in the outer rims. The juvenile clinopyroxenes in the studied rocks are of titaniferous diopside composition, explaining the observed anomalous interference colours.

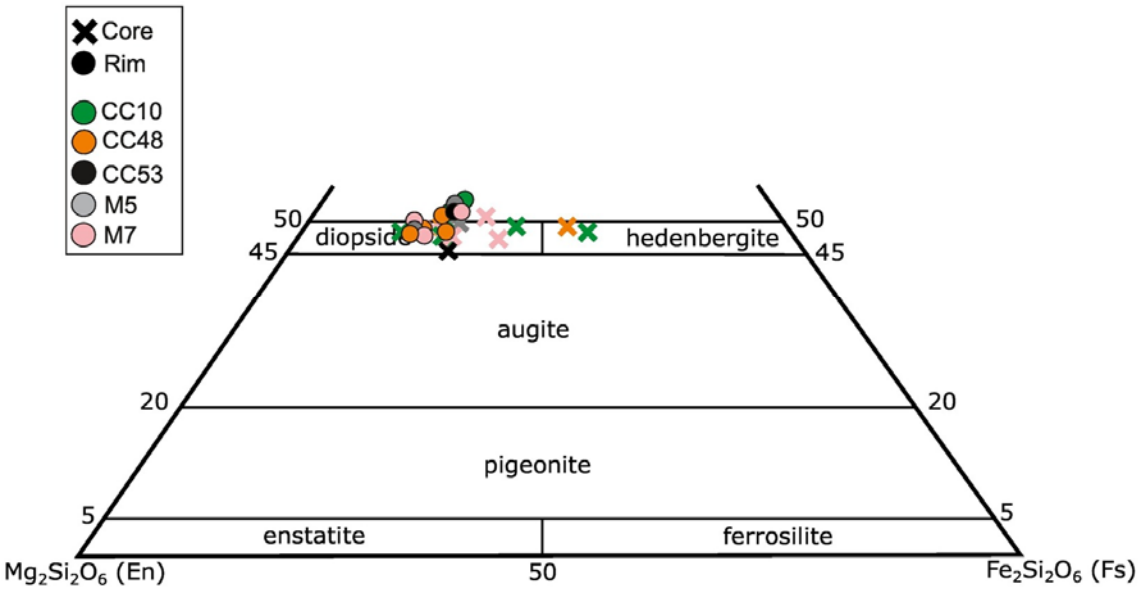

Fig. 4. Classification of selected pyroxene cores and rims.

In phenocrysts with anhedral cores, the cores of clinopyroxene composition exhibit Mg# of 48–68 while the inner juvenile rims exhibit Mg# of 77–74. Thus, they are less mafic than the rims. If we include the composition of one of the unmantled cores in samples from eruption centres DX1 and CC10 (sample B05), the range of compositions of these cores is even extended to Mg# as low as 42–39. Na varies in the cores between 1 and 2% with the higher values being accompanied by an increase in Fe but not in Al. Lherzolitic orthopyroxenes (Mg# 62, CaO 0.06 wt%) and Cr-diopsides (Mg# 86, Cr_2O_3 and TiO_2 0.97 wt% each) were only rarely measured as anhedral cores.

In the backscatter images of phenocrysts with reverse zoning from xenomorphic cores to euhedral rims, a marked colour change can be noticed between uniform light grey cores and the dark grey rims that are getting less dark outwards. This reflects the marked decrease of FeOt contents at a sharp boundary (Fig. 5A). Only in the core analyses closest to this boundary, the Mg# are slightly enriched. Within the rims, the Mg# decrease outwards to Mg# 70. When we measured a sieve textured core, all individual crystals replacing the primary core exhibited a Mg# of 77–75, which was identical to the composition of the inner rim (Fig. 5B). Within the rims of these phenocrysts, the Mg# decrease outwards to Mg# 70.

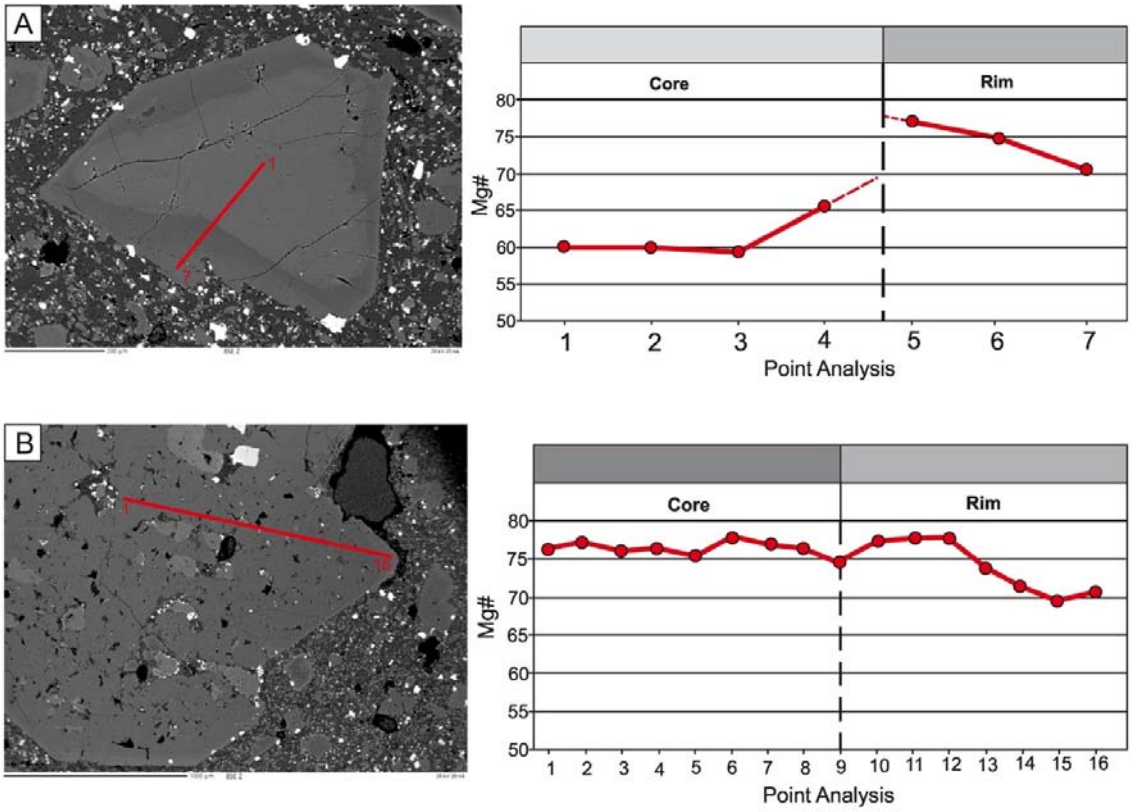

Fig. 5. A) Line analysis of a clinopyroxene, showcasing oscillating Mg# values of the crystal's interior transitioning to a lower Mg# rim. B) Line analysis of a clinopyroxene cumulate that showcases reverse zoning.

4.2.3. Plagioclase

Plagioclase is the major leucocratic mineral within the samples that only occurs in the matrix. Only for documentary reasons, we measured 8 representative plagioclase minerals. The compositions in the basanites range from *An* 72 to 69 (bytownite/labradorite), in the hawaiite from *An* 64 to 54 (labradorite). The contents of K_2O are low, ranging from 0.22–0.25 wt% in the basanites and from 0.25–0.32 wt% in the hawaiite, which is only slightly higher.

4.3. Whole rock geochemistry

Of the 44 analysed samples, we removed those with normative *hy* (6 samples) as this characteristic contradicts the observed juvenile set of solidus phases. Thus, the used data include analyses of 38 samples from 16 volcanoes. The Chemical Index of Alteration (CIA) (Nesbitt and Young, 1982) values of the BMVF rocks, ranging from 44 to 54% (average = 50%), in conjunction with low loss on ignition (LOI) values of <2%, indicate that the samples did not experience significant weathering (Appendix A, Table 1).

4.3.1. Major and trace elements

Major and trace element data for the volcanoes are reported in Appendix A, Table 1 and are visually represented in Figures 6-9. Major elements are recalculated to 100 wt.% on an anhydrous basis with total Fe as Fe_2O_3t. The rocks in the BMVF exhibit SiO_2 contents that

range from 41 to 48 wt% (avg. = 43 wt%) (see Appendix A, Table 1). SiO_2 vs. total alkali contents (K_2O + Na_2O range between 4.1 and 6.3 wt%, on average 5 wt%) indicate that the lava flows and tephra of the BMVF are dominantly basanitic in composition (Fig. 6); the calculated Mg# (Mg# = molar [MgO/(MgO + FeO)]) vary between Mg# 53-72 (Mg# 64 on average). Three analyses, two of cinder cone CC6 and one from maar M11, exhibit higher alkali and SiO_2 contents. Two of these (CC6) still fall into the tephrite/basanite field close to the boundary to the hawaiite field in which the third analysis plots. All three analyses are additionally characterised by lower contents of CaO, Fe_2O_3t, TiO_2 and P_2O_5, paired with increased contents of Al_2O_3. However, only the hawaiite (M11) exhibits a lower MgO content.

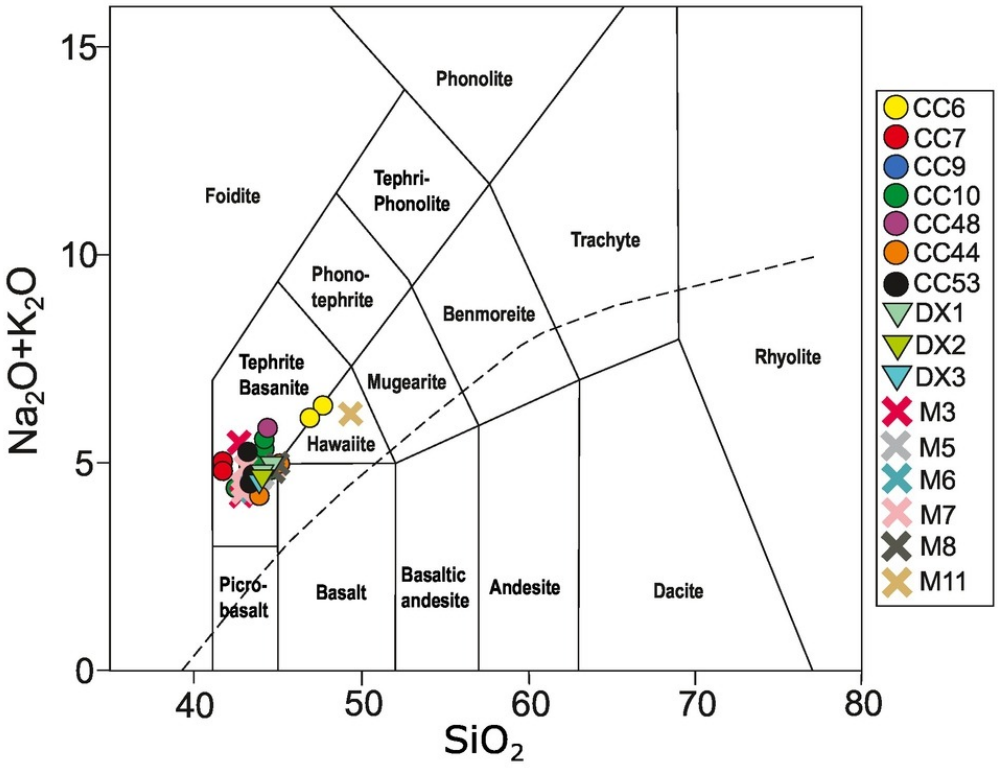

Fig. 6. TAS diagram Le Maitre et al. (2002) of the BMVF with the fields "Hawaiite", "Mugearite" and Benmoreite" (see text). Alkaline/subalkaline division line after Irvine and Baragar (1971).

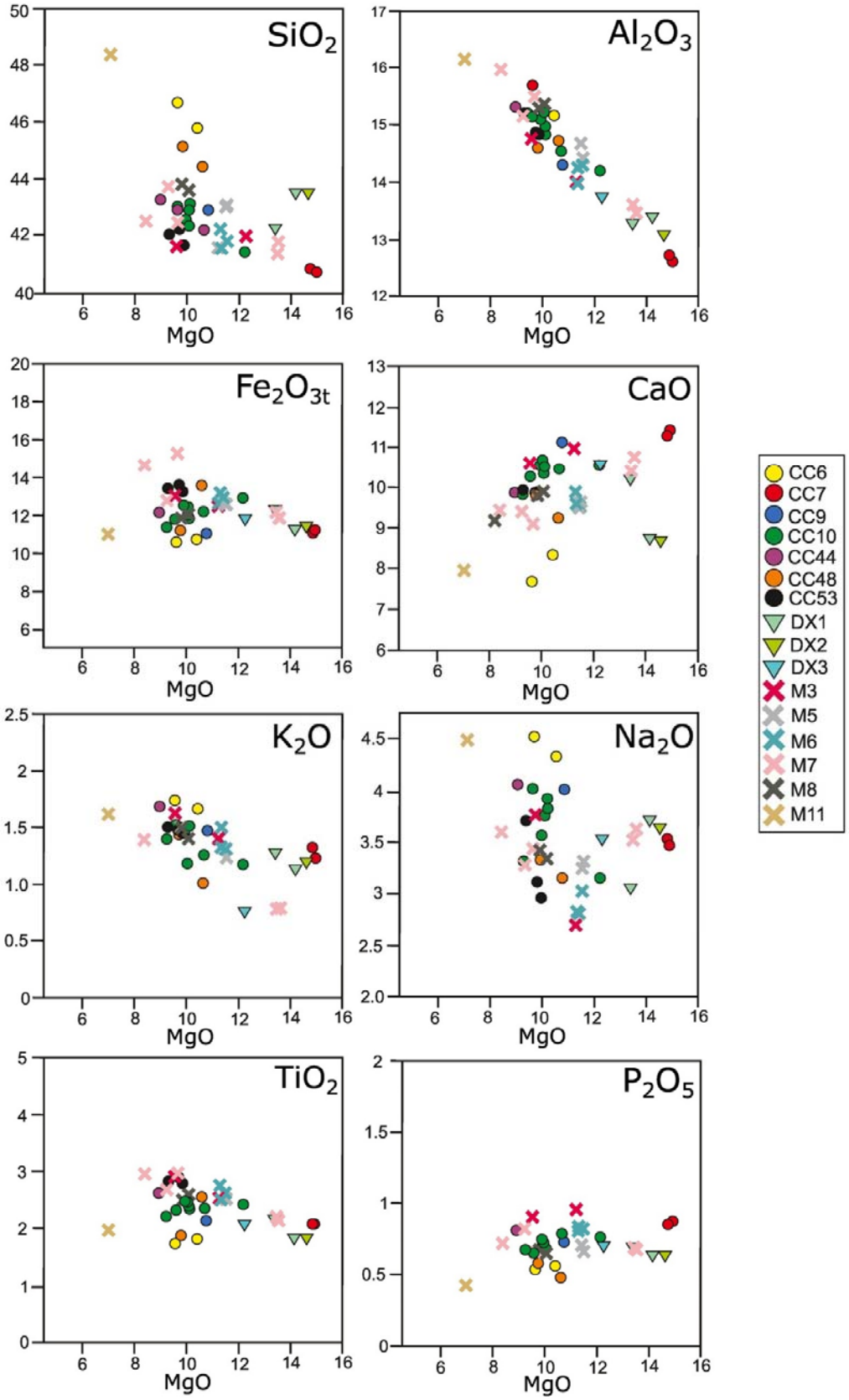

Fig. 7. Major element oxide variation diagrams of the BMVF rocks.

Major element variation diagrams (Fig. 7) use MgO as abscissa as it illustrates best the compositional variation in the mafic rocks of the BMVF. The compositional trends that are visible with decreasing MgO can be grouped into those that exhibit (1) a steady increase, reflecting incompatibility (Al_2O_3, K_2O), (2) a steady decrease, reflecting compatibility (CaO), (3A) a slight increase followed by a decrease in the hawaiite, reflecting semi-compatibility (Fe_2O_3t, TiO_2, P_2O_5), (3B) indifferent variation down to 11 wt% MgO with a sharp increase below semi-compatibility (SiO_2, Na_2O). The analyses for CC6 would fit these patterns if they would be characterised by 8 wt% MgO. Deviations of ~2% from these trends are also shown by one analysis each of the lava flows DX1 and DX2 with respect to SiO_2 and CaO at 14.2 and 14.6 wt% MgO, respectively. The majority of the samples, including those of CC6, are characterised by MgO contents of 9–11 wt% and exhibit the widest range of variations of the other major and minor elements, e.g., from 1.8 to 3.0 wt% for TiO_2, 10.6 to 15 wt% for Fe_2O_3t, and 2.7 to 4.5 wt% for Na_2O.

Selected trace element data of the BMVF (see Appendix A, Table 1 for complete data set) are plotted on variation diagrams with MgO taken as abscissa (Figs. 8A and B). A positive trend with declining MgO contents is portrayed by Ni and Cr, reflecting their compatibility. Sc exhibits a semi-compatible variation that slightly increases from 15 to 9 wt% MgO. However, a group of analyses is characterised by values of more than 40 ppm at 9–11 wt% MgO (further referred to as the high-Sc-group, consisting of individual samples of M8, CC10 and CC53); an additional high Sc sample is visible at 15 wt% MgO (one sample of CC7). The HREE, represented by Yb, shows an overall incline with declining MgO, which does not continue towards the hawaiite that exhibits slight semi-compatible behaviour. The outlier group that is defined by high Sc is also visible in the Yb diagram. However, one sample from CC6 without high Sc also exhibits high Yb contents. The remainder of the trace elements seems not to show differentiation trends (Fig. 7B). However, this is mainly due to the variable enrichment of trace elements, including the HFSE, LREE and LILE in samples with MgO >14 wt%, which are defined as cumulates, based on the Fo% of olivines (see below). Excluding these as well as the two analyses of CC7, the values for HSFE, LREE and LILE show a slight increase with declining MgO. At 10 ±1 wt% MgO, this is camouflaged by an increased variation of the elements, some of which is due to higher values in samples of the high-Sc-group; this is best illustrated in the Sr vs. MgO diagram. The two samples from CC7 are characterised by an enrichment of all of these elements, except for Zr.

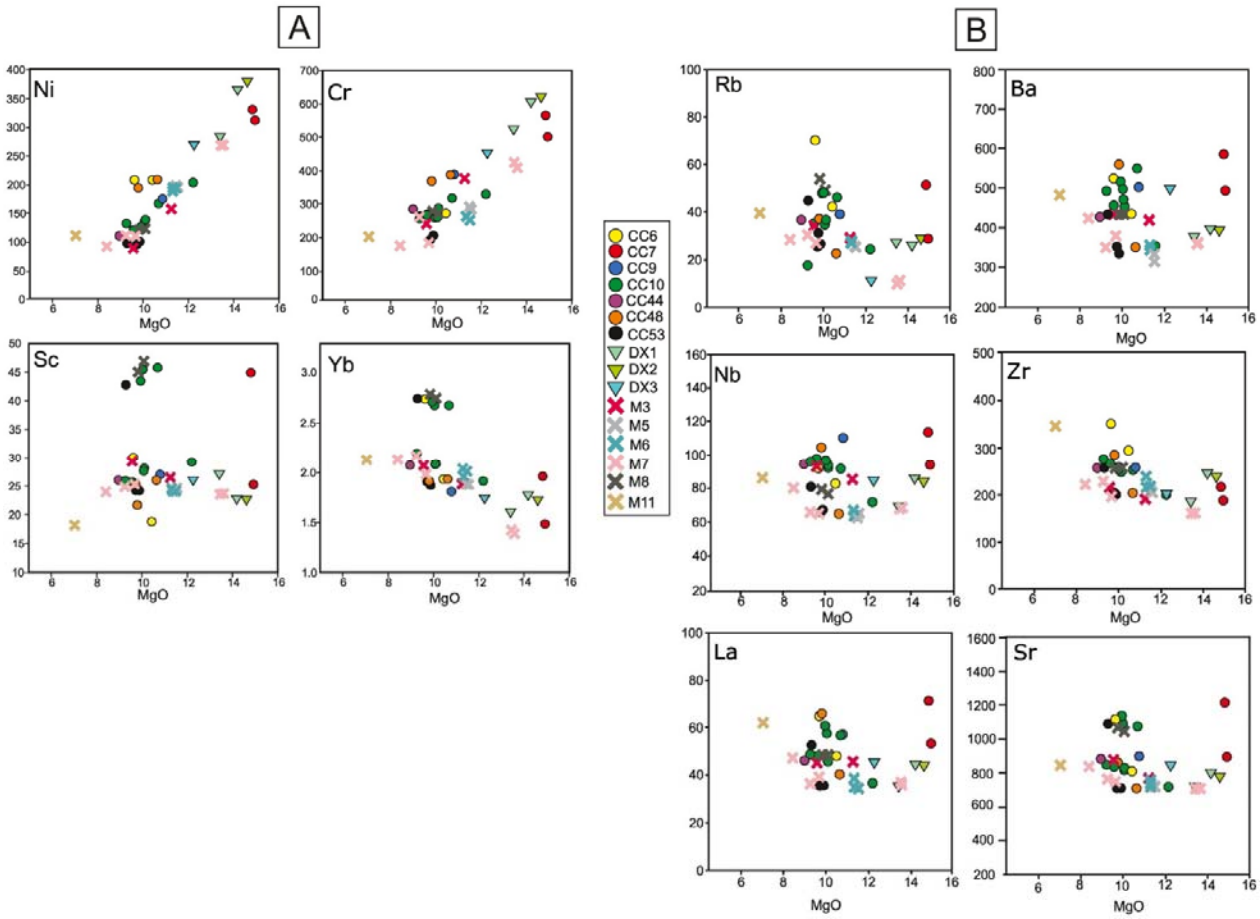

Fig. 8. A) Compatible, semi-incompatible and B) incompatible trace element variation diagrams of the BMVF rocks.

In a C1 chondrite-normalised REE diagram (Fig. 9A), the ratios uniformly decrease from 130 to 300 for La to 8–18 for the HREE Tm to Lu. Thus, the sub-parallel patterns are described to be LREE-enriched and HREE-depleted; they are comparable to patterns of OIB.

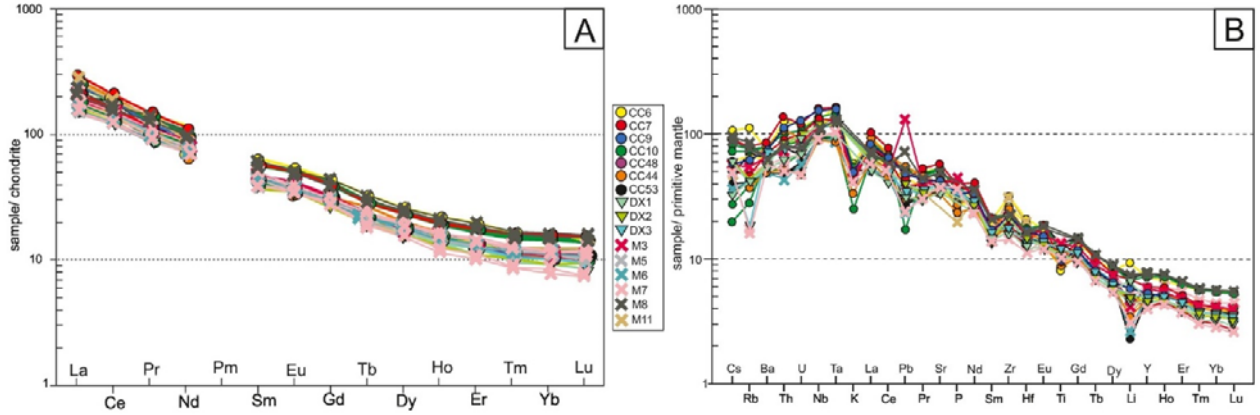

Fig. 9. A) C1 chondrite-normalised Rare Earth Element (REE) diagram (Sun and McDonough, 1989). B) Primitive mantle-normalised spider plot (Sun and McDonough, 1989) of the BMVF.

In a primitive mantle-normalised trace element diagram (Fig. 9B), we included selected trace, minor and major elements (Cs, Rb, Ba, Th, U, Ta, K, Pb, Sr, P, Zr, Hf, Ti, and Y) and put them in the order according to Lustrino and Wilson (2007). Li was placed according to the recommendation by Sun and McDonough (1989). The trace element abundances of the BMVF rocks match the pattern of OIB (Sun and McDonough, 1989), especially with respect to the REE. The highest enrichment is shown by Nb and Ta ratios (80–160). The normalised concentration patterns exhibit a minor negative trend from Nb to Cs as well as a strong negative trend from Ta to Lu. The ratios of the REEs and some trace elements such as Ba, Nb, Ta, K, Sr, Hf, Ti, and Y are rather uniform and vary only by a factor of two. Other trace element ratios display larger variation, e.g., Cs, Rb, Pb, and Li. Negative anomalies of K, Pb, Sm and Li are shown by all analyses while only some samples that are low in MgO exhibit minor negative anomalies for the elements P and Ti. Cs and Rb are depleted with respect to Ba, while a small number of analyses exhibits a negative Ba anomaly. The apparent negative anomaly of Sm only results from Sm not being placed in order of decreasing bulk partition coefficients for garnet-lherzolite as a measure of incompatibility as suggested by Sun and McDonough (1989). The other negative anomalies will be discussed in section 5.1.

4.3.2. Sr, Nd, Hf and Pb Isotopes

The Sr, Nd, Hf and Pb isotope ratios of the 10 analysed samples are reported in Table 2 of Appendix A. The ratios of the BMVF do not show large variation in Sr, Nd, Hf and Pb isotope correlation diagrams (Fig. 10). The $^{87}Sr/^{86}Sr$ ratios of seven out of ten samples with MgO contents of 15–9.5 wt% show uniform values of 0.703132–0.703184 with an average of 0.703173. Only 3 samples with MgO contents of 10–7 wt% show larger deviations of ±0.0002, ranging from 0.703010–0.703347 (Fig. 10A, B and E). $^{143}Nd/^{144}Nd$ ratios range from 0.512869–0.512995 (avg. = 0.512904) with εNd (normalised to Bouvier et al., 2008) values varying accordingly between +4.5 and +5.9 (Fig. 10A and D). $^{176}Hf/^{177}Hf$ ratios range from 0.283006–0.283026 (avg. = 0.283017) with εHf values varying accordingly from +7.8 to +8.5 (Fig. 10D, E and F). The Pb isotope dataset of 6 samples contains one outlier (sample V07 of volcano M8). This sample is not included in calculating the following avg. values: $^{206}Pb/^{204}Pb$ ratios range from 19.787–19.895 (avg. = 19.861) (Figs. 10B, C and F), $^{207}Pb/^{204}Pb$ ratios range from 15.656–15.653 (avg. = 15.647), and $^{208}Pb/^{204}Pb$ ratios range from 39.560–39.678 (avg. = 39.628) (Fig. 10C).

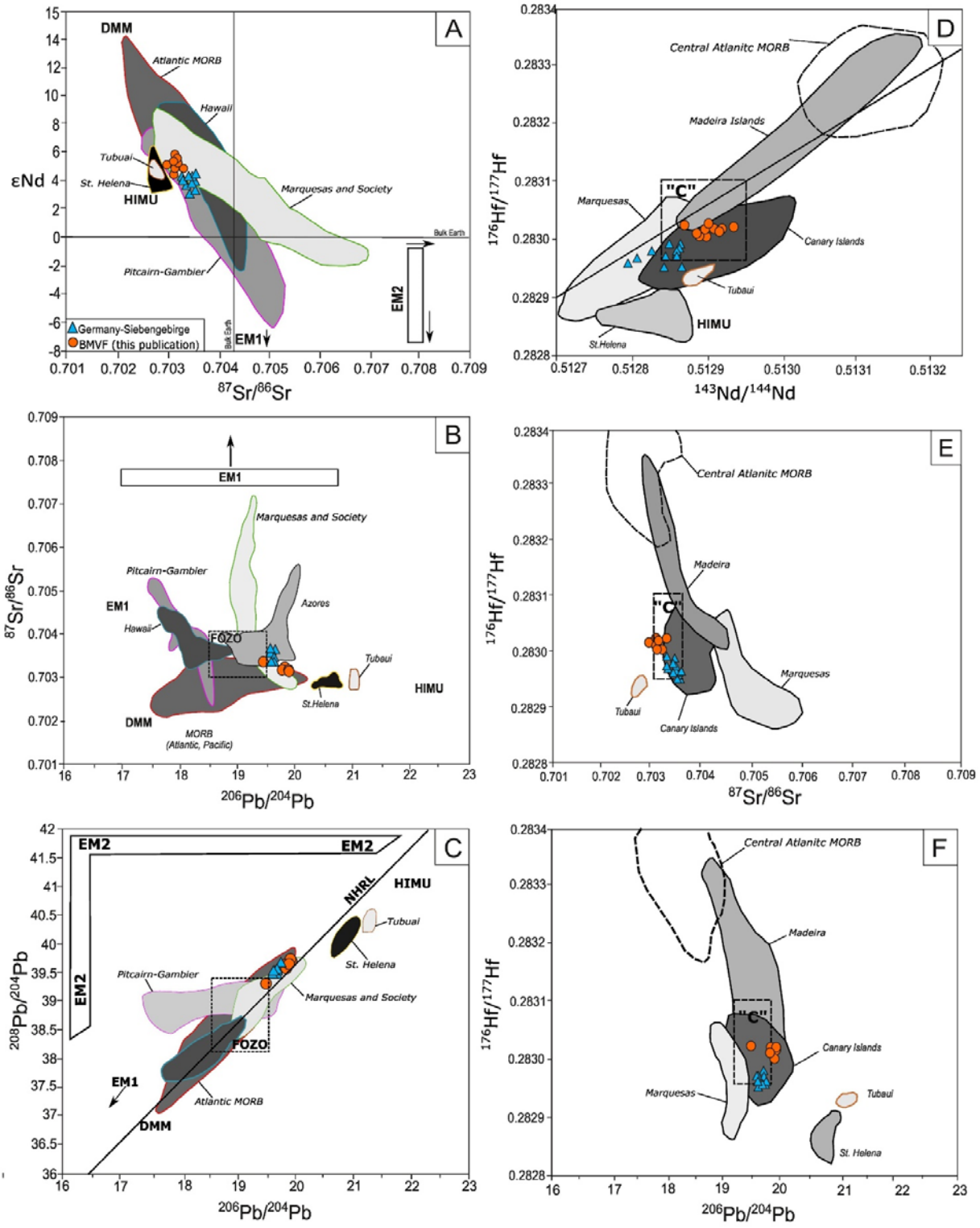

Fig. 10. Isotope ratios of the BMVF samples, plotted together with the mantle endmembers DMM, EM1, EM2, HIMU, FOZO and "C" (see text for references) in addition to reference fields from Chauvel et al. (1992); Hofmann et al. (2003); Bizimis et al. (2003). A) εNd vs. $^{87}Sr/^{86}Sr$ diagram, B) $^{206}Pb/^{204}Pb$ vs. $^{87}Sr/^{86}Sr$, and C) $^{206}Pb/^{204}Pb$ vs. $^{208}Pb/^{204}Pb$. The Georoc database (http://georoc.mpch-mainz.gwdg.de/georoc/) and Geldmacher et al. (2011) and references therein were utilised for reference fields in the $^{176}Hf/^{177}Hf$ diagrams: D) $^{143}Nd/^{144}Nd$ vs. $^{176}Hf/^{177}Hf$, E) $^{87}Sr/^{86}Sr$ vs. $^{176}Hf/^{177}Hf$, and F) $^{206}Pb/^{204}Pb$ vs. $^{176}Hf/^{177}Hf$.

In order to contextualise the isotopic signatures of the BMVF rocks, we compared them with global reference fields, a selection of data from the mid-Atlantic Ocean ridges as well as groups of ocean islands (Hawaii, Marquesas-Society, Pitcairn-Gambier) and individual ocean islands (St. Helena and Tubuai) (Hofmann, 2003, and references therein; http://georoc.mpch-mainz.gwdg.de/georoc). In addition, isotope ratios of mantle endmembers are given: FOZO for Focus Zone according to Hauri et al. (1994), "C" as defined as Common Mantle by Hanan and Graham (1996), DMM - Depleted MORB Mantle as well as EM1 and EM2 as Enriched Mantle endmembers as defined by Zindler and Hart (1986), HIMU endmember (high $\mu = {}^{238}U/{}^{204}Pb$) according to Chauvel et al. (1992).

In terms of εNd compared to $^{87}Sr/^{86}Sr$ ratios (Fig. 10A), the BMVF samples plot into the quadrangle of mantle values and are neighboured by the German volcanic field of the Siebengebirge. Both fall within the field of the FOZO endmember and overlap with the low $^{87}Sr/^{86}Sr$ ends of the Marquesas-Society and Pitcairn and Gambier reference fields. Lying at the lower end of the Atlantic MORB ratios, they are enclosed by the reference fields of Tubuai and St. Helena on the low $^{87}Sr/^{86}Sr$ side and Hawaii on the high $^{87}Sr/^{86}Sr$ side.

In terms of $^{87}Sr/^{86}Sr$ compared to $^{206}Pb/^{204}Pb$ (Fig. 10B), the BMVF samples plot on a line between the FOZO and the HIMU endmembers on the low $^{206/204}Pb$ side of St. Helena and Tubuai. With one exception the analyses form a well-defined cluster, which is accompanied by the cluster of the Siebengebirge.

In terms of the comparison of $^{208}Pb/^{204}Pb$ to $^{206}Pb/^{204}Pb$ (Fig. 10C), the data from the BMVF and the Siebengebirge display tight groupings between the FOZO and the HIMU on the Northern Hemisphere Reference Line (NHRL) (Hart, 1984). Similar to Fig. 10B, one BMVF sample plots with lower $^{206}Pb/^{204}Pb$ values into the FOZO field.

In order to compare the $^{176}Hf/^{177}Hf$ with the $^{143}Nd/^{144}Nd$ ratios (Fig. 10E), the BMVF samples exhibit a wide range of Nd values and a small range of Hf values at >0.2830. For reference, only data from the Tubuai, St. Helena, Marquesas, Madeira and Canary Islands, as well as MORB from the central Atlantic were available and were used in Fig. 10 D–F. As data for the FOZO are not available, we used the data for the common mantle endmember as defined by Hanan and Graham (1996) as "C". The BMVF data plot within the overlap of data from Madeira, and the Canary and Marquesas islands within the field of "C". The range is slightly offset from the mantle array to lower Hf ratios, which is also true for the less well-defined group of data from the Siebengebirge.

Comparing the $^{176}Hf/^{177}Hf$ with $^{87}Sr/^{86}Sr$ ratios (Fig. 10E), the data for both the BMVF and the Siebengebirge plot into the "C" field with some overlap with the Canary Islands data. For this pair of ratios reference values for St. Helena are not available.

Comparing the $^{176}Hf/^{177}Hf$ with $^{206}Pb/^{204}Pb$ ratios (Fig. 10F), the data for both the BMVF and the Siebengebirge overlap with the Canary Islands data. Both data sets plot on the edges of the common mantle endmember "C" to higher Pb values relative to the Marquesas Islands; the BVMF data show a minor overlap with the data from Madeira Island.

5. Discussion

5.1. Melt generation and differentiation

The major and trace element variations of the BMVF samples follow typical differentiation trends that are consistent with the observed phenocryst assemblages (Fig. 7, Fig. 8). Decreasing concentrations of MgO (Fig. 7), Cr and Ni with increasing Al_2O_3 are related to the fractionation of olivine, clinopyroxene and spinels of the chromite series (seen as inclusions and individual crystals in the basanites). A decrease in CaO with increasing Al_2O_3 is also controlled by clinopyroxene fractionation. This is in agreement with the observation that plagioclase only occurs as a matrix phase in all basanites and the hawaiite. However, the assemblage of fractionating phases changes during the increasing degree of differentiation of the series as indicated by changes from enrichment to depletion of semi-compatible elements: SiO_2 and Na_2O increase at ≤10 wt% MgO, which is accompanied by a decrease of Fe_2O_3t, TiO_2 and P_2O_5 as well as a steepening of the slope of CaO depletion below 9 wt% MgO. This reflects the combined effect of fractionating Fe–Ti oxide minerals as well as apatite.

Within this differentiation series, some samples show unsystematic element deviations: (1) the samples with higher MgO than 14 wt%, (2) the two samples of cinder cone CC6, and (3) the samples exhibiting high element variations at 10 ±1 wt% MgO, which include (4) the high-Sc-group.

(1) Based on the highest NiO-contents of the olivine phenocrysts, we calculated the most primitive melts of the differentiation series, characterised by Mg# 69 and based on $(Fe–Mg)^{ol\text{-}liq}$ values of 0.30 ±0.03 (or ±1σ) (Roeder and Emslie, 1970). This value is equivalent to less than 14 wt% MgO in the BMVF series. Thus, all analyses exhibiting higher MgO contents than 14 wt% are interpreted as cumulates. The cumulates are characterised by slight or marked enrichment of HSFE, LILE and LREE, indicating a higher degree of differentiation (see samples from lava flows DX1 and DX2 and cinder cone CC7, Fig. 8A and B), and formed due to an accumulation of up to ~10% of olivine and clinopyroxene to a basanite with 10 wt% MgO, as necessitated by their high Ni- and Cr-contents.

(2) The two samples from CC6, which plot in the TAS diagram into the differentiated basanite field (Fig. 6), are characterised by high concentrations of incompatible elements, e.g., Si, Na and Zr. However, they are offset from the above-described variation by 2 wt% MgO and 100 ppm Ni. Thus, we interpret the two samples as tephrites, which experienced 4% of olivine addition.

(3) The dataset is characterised by a large variation in the contents of incompatible elements (Fig. 8B). This may be explained by AFC processes that are complicated by (a) mingling and (b) mixing processes between more or less differentiated melts accompanied by (c) assimilation of country rock:

(a) Mingling is common in the BMVF and described from samples M6, CC10, CC44 and CC48 as contacts between melts of different crystallinity. (b) Mixing is a common process that is indicated by anhedral cores of olivines and especially clinopyroxenes. The anhedral xenocrystic cores of the clinopyroxenes comprise co-magmatic clinopyroxenes as well as

lherzolithic orthopyroxenes and Cr-diopsides. The often green coloured or sieve textured co-magmatic clinopyroxenes grew in higher differentiated magmas than the juvenile Ti-diopsides that are mantling them. The compositions of the juvenile clinopyroxenes range from Mg# 78–67 with increasing Ca and Ti contents outwards, reflecting the changing melt compositions during differentiation. Some sieve-textured clinopyroxene xenocrysts are even unmantled (in cinder cones CC10 and CC44), indicating incorporation only prior to the eruption. In contrast, unmantled xenocrysts in tephra samples from maars are interpreted to be incorporated during phreatomagmatic explosions (e.g., quartz in M8).

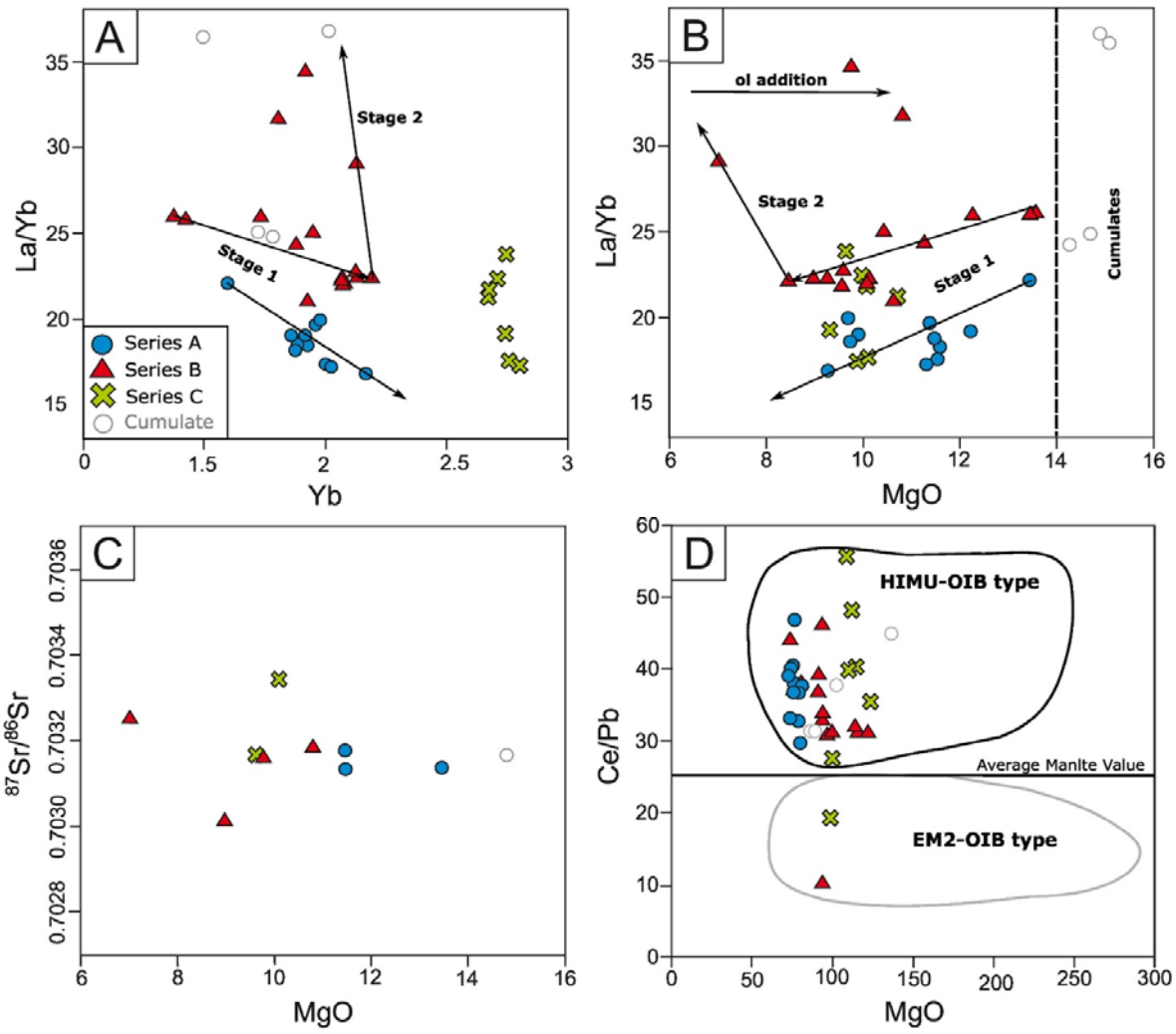

Fig. 11. The three magma series of the BMVF and related differentiation mechanisms are shown in A) La/Yb vs. Yb diagram and B) MgO vs. La/Yb. C) MgO vs. $^{87}Sr/^{86}Sr$ and D) Ce/Pb vs. MgO show the HIMU-OIB type character of the BMVF (see text for references).

(c) Crustal and mantle xenoliths in the BMVF were described by Lucassen et al. (2008a) and Lenhardt et al. (2018). On a microscopic scale, we see individual resorbed xenocrysts of lherzolithic orthopyroxene and Cr-diopsides as well as garnet, Al-spinel/uvoravitic garnet, MgFe-mica (Lucassen et al., 2008) and plagioclase, proving that assimilation of mantle and crustal rocks did occur. However, the constancy of $^{87}Sr/^{86}Sr$ with decreasing MgO from 15 wt% down to 9 wt% in 7 out of 10 analysed samples proves that assimilation did not have an

adverse chemical effect on most of the samples (Fig. 11C). The samples that show deviations are characterised by MgO contents of 10–6 wt%.

(4) In the same more differentiated interval of the basanites with 9–11 wt% MgO, a group of magmas forms a separate group with a peculiar combined enrichment in LILE and REE (Fig. 8A). It is most prominently characterised by enrichment of Sc and Yb and referred to as high-Sc-group. When plotted in a LREE/HREE vs. HREE diagram (Fig. 11A), the samples of this high-Sc-group, here addressed as Series C, can be clearly distinguished from all other samples. The correlation diagram also allows distinguishing the remaining samples into one group with low La/Yb ratios (Series A) and another group with high La/Yb ratios (Series B) at comparable Yb contents. A comparison with MgO of the samples indicates that the samples follow two parallel differentiation trends (Fig. 11B). The two highly differentiated samples in Series B are offset to higher MgO due to olivine addition.

When comparing the chondrite-normalised REE patterns of these series, both are characterised by LREE-enriched and HREE-depleted patterns. However, the Series B magmas show higher enrichment in LREE (Fig. 12A). We interpret this difference to be due to different degrees of partial melting of the two magma series from an identical garnet-bearing mantle source (see below).

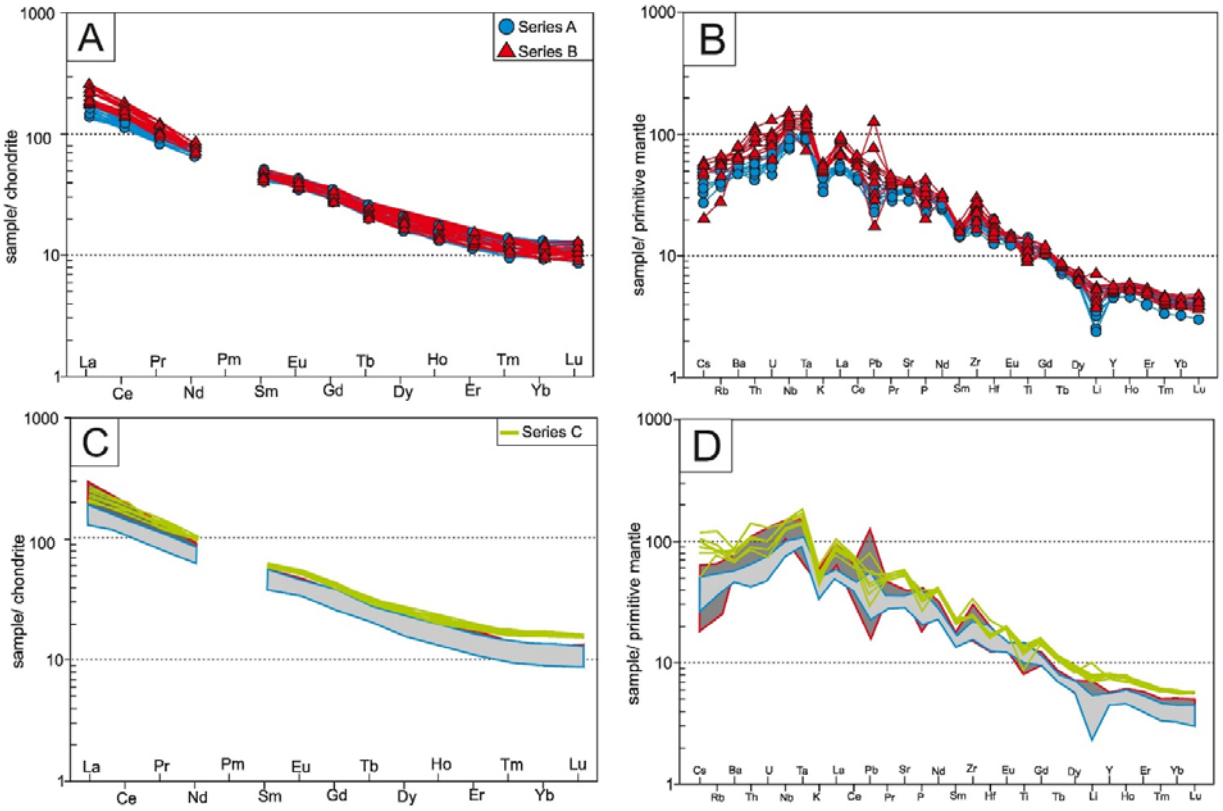

Fig. 12. A) and C) C1 chondrite--normalised REE diagrams (Sun and McDonough, 1989), B) and D) Primitive mantle-normalised spidergrams (Sun and McDonough, 1989): B) illustrating the general enrichment of Series B relative to Series A and D) trace element concentrations of Series C superimposed over Series A and B, displaying similar and enriched signatures relative to Series B.

Magmas of Series C also exhibit the LREE-enriched and HREE-depleted patterns that require garnet as a residual phase in the mantle source. However, they are enriched in the whole set of REE with respect to samples of Series A (Fig. 12C). As they exhibit the same MgO contents as the basanites of Series A, they cannot be more differentiated by fractional crystallisation processes. Therefore, we interpret this parallel offset to higher ratios of REE to be due to a mixing of rising magmas of Series A composition, intercepting with stalled magma pockets/mush zones that must have been hosted in the crust. Compared to Series B, Series C exhibits the same LREE ratios but higher ratios for HREE.

Comparing the samples from Series A to C in a spidergram, we see that all patterns are characterised by the highest enrichments shown for Nb and Ta, associated with negative anomalies of K, Pb and Li. Only samples of Series A additionally exhibit a moderate Th–U trough. Comparing the samples from Series A and B, with one exception in each series, those sampled from Series B are characterised by an enrichment not only in the LREE but also in all incompatible elements from Cs to Ta by a factor of 1.5–2. Series C samples are different from those of Series A by marked enrichments in Cs to Ta, the REE as well as Sr and Li; identical are only the ratios of K, Pb, P, and Ti.

The K-anomaly (expressed as K_N/K_N* where $K_N^* = \sqrt{(Ta_N \times La_N)}$) is pronounced in all three series, being the least pronounced in Series A with 0.7 and grading over Series B into Series C with values below 0.5 (Fig. 13A). Within Series A and B, the anomaly decreases slightly with increasing differentiation. The Pb-anomaly (expressed as Pb/Pb_N^* where $Pb_N^* = \sqrt{(Ce_N \times Pr_N)}$) is less pronounced, varying between 0.5 and 1.0 and being almost indistinguishable between the different series (Fig. 13B). The Pb-anomaly, expressed by Ce/Pb ratios larger than 25, allows characterising all sampled rocks (except for two outliers) as being of HIMU-OIB type (Chauvel et al., 1992) (Fig. 11D). The Li-anomaly (expressed as Li/Li_N^* where $Li_N^* = \sqrt{(Y_N \times Dy_N)}$) develops during differentiation and is more pronounced in Series A (Fig. 13C). Erratic values occur in all diagrams but are more common in samples of Series B and C.

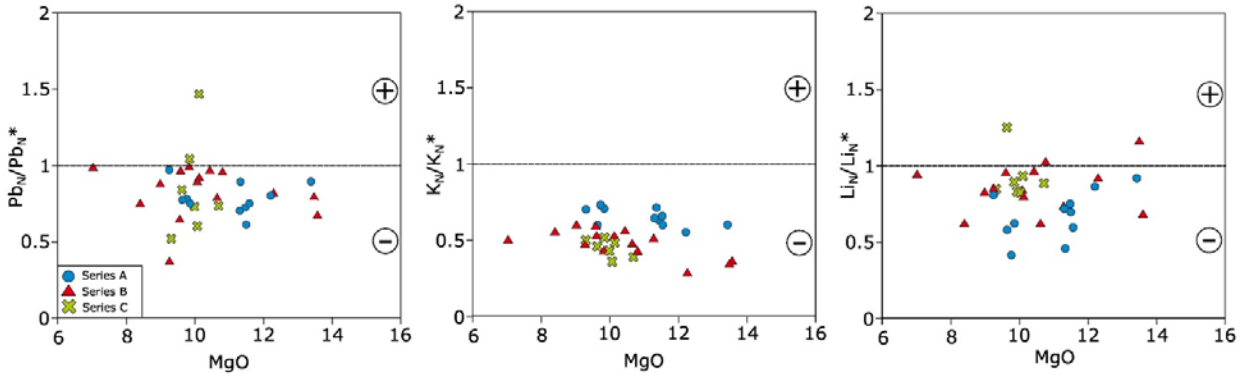

Fig. 13. Negative anomalies of Pb, K and Li. A) Pb_N/Pb_N^*vs. MgO, B) K_N/K_N^*vs. MgO, C) Li_N/Li_N^* vs. MgO (see text for explanation).

Thus, the primitive mantle-normalised trace element patterns of all samples resemble a HIMU-OIB type character that is attributed to the presence of garnet (depleted HREE patterns) and the negative Pb-anomaly.

The depleted HREE patterns indicate that garnet must have been a residual phase in the mantle source during melt generation as the HREE, represented by Yb, have high partition coefficients to garnet ($K_d^{Yb}{}_{garnet}$ = 5.5 at 3.0 GPa; Salters and Stracke, 2004). The Yb content is buffered (Yb at ~2 ppm in the BMVF samples) as the degree of melting increases. Garnet in the mantle provides constraints to the pressure, and therefore depth, at which the melt was generated. The garnet/spinel transition zone, increasing to higher pressures with increasing temperature, is experimentally determined at ca. 2.0–2.2 GPa and 1200–1300°C, crossing the field of experimentally determined pT-conditions that are needed for the generation of mafic melts of basanitic composition from water-saturated peridotites (pyrolite) (Green et al., 1974; Green and Falloon, 1998; O'Hara et al., 1971). This forms the minimum pressure at which the BMVF melts formed.

The additionally distinctive K-trough, characterising all samples from the BMVF in the primitive mantle-normalised spidergram, is indicative of the presence of a hydrous phase (amphibole or phlogopite) in the mantle source. Under anhydrous conditions of a peridotitic mantle, K and LREE and HFSE such as Nb and Ta are equally incompatible and should therefore act similarly during progressive melting, e.g. indicated by a constant K/Nb or K/La ratio. However, if a hydrous mineral phase such as amphibole or phlogopite is present in a mantle that has been infiltrated by fluids (metasomatised) any time prior to melting (Class and Goldstein, 1997; Späth et al., 2001), K acts more compatible than e.g., Nb ($K_d^{K,Nb}{}_{amphibole}$ = 0.8, 0.069 according to Adam and Green (2006) and $K_d^{K,Nb}{}_{phlogopite}$ = 3.67, 0.088 according to LaTourrette et al. (1995), respectively). This retainment of K by a hydrous phase during melt generation of the Bayuda magmas is indicated by the negative K-anomaly (expressed as K_N/K_N* values <1) where $K_N* = \sqrt{(Ta_N \times La_N)}$ is the inferred normalised K concentration of rocks that are derived from an unmetasomatised mantle while K_N represents the normalised, measured concentration of the rocks. Series A display less pronounced K_N/K_N* of 0.57-–0.69 than samples of Series B with values of 0.29-–0.60. This indicates that the negative K anomaly decreases with lager partial melting fractions. It is worth noting that K is increased by fractional crystallisation due to being incompatible with respect to the crystallising phases olivine, clinopyroxene and Fe–Ti oxides.

The differences in incompatible element ratios based on the hydrous mantle source composition can be explained by a melting model (Fig. 14B). Due to compositional similarities, our melting model (based on Duggen et al., 2005) uses the partition coefficients given by Altherr et al. (2019) (shown in Appendix A, Table 4). Garnet lherzolite, phlogopite-garnet lherzolite, amphibole-garnet lherzolite, spinel lherzolite, and amphibole-spinel lherzolite were selected as potential mantle sources. Melting curves represent non-modal batch melting (Shaw, 1970) where pyrolite (PUM) (McDonough and Sun, 1995) was used as a starting composition and Dy = 0.19 and Yb = 0.12 were selected as mantle source compositions using the reasoning of Kolb et al. (2012) for the Siebengebirge. The selected values plot within the reported compositions of the metasomatised mantle of the Hessian Depression (Hartmann and Wedepohl, 1990), which could also be a source characteristic of the lithospheric mantle beneath the BMVF. The non-modal batch melting curves suggest that both parental melts of Series A and B formed through partial melting of an amphibole-bearing garnet lherzolite. The calculations for magmas with Mg# 69 plot between compositions of amphibole-garnet and amphibole-spinel lherzolite. The best results are gained for calculations using samples with Mg# 64–65 (6% for Series A and 4% for Series B).

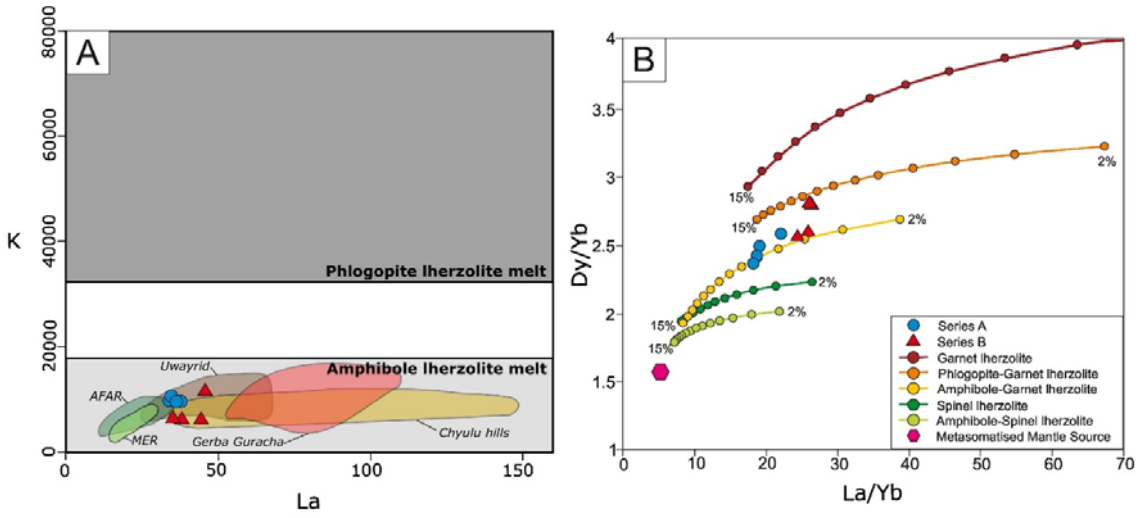

Fig. 14. A) K vs. La diagram demarcating the La and K content fields of an amphibole-garnet lherzolite and a phlogopite-garnet lherzolite (Späth et al., 2001). Included reference fields: Afar and MER fields (Ayalew et al., 2016), Uwayrid (Altherr et al., 2019), Gerba Guracha (Rooney et al., 2014) and Chyulu hills (Späth et al., 2001). B) Dy/Yb vs. La/Yb non-modal batch melting curves of four selected source lithologies, indicating partial melting of a garnet-bearing source rock (see Appendix A, Table 4 for model parameters).

5.2. An integrated plumbing model

The plumbing system of polygenetic volcanoes refers to the network of subsurface magma-filled dykes, chambers and conduits of variable complexity that interconnect and lead to the surface volcanic structure. The plumbing system of a monogenetic volcano can be relatively simple due to its singular eruptive nature and primitive compositions. However, as more monogenetic volcano plumbing systems are studied, it is becoming apparent that they can be more intricate (Coote et al., 2019; Németh et al., 2003; Németh and Kereszturi, 2015). Németh et al. (2003) suggest that a compositional variation in monogenetic volcanoes can be explained by means of emplacements of small, stalled magma systems of varying spatial and temporal characteristics within the crust. The proposed model for the BMVF follows the same reasoning (e.g., Coote et al., 2019).

The BMVF is characterised by two different magma series of basanite, Series A and B, that show minor differentiation. Only Series B developed to tephrites (volcano CC6) and hawaiite (volcano M11) (Fig. 1C). The basanitic rocks of Series A and B cannot be distinguished based on petrographic or minerochemical data. A third series, Series C, could have been differentiated from one of the erupting series (Series A), however, not by fractional crystallisation to tephrite or hawaiite. The melts of Series C rather formed by rising magma intercepting with stalled magma pockets/mush zones that were hosted in the crust.

The range of compositions in pyroxenes present in the BMVF suggests the presence of at least one magma storage system common for all three series with respect to early conditions. The anhedral, resorbed, partially/completely replaced (sieve textured) cores of clinopyroxene in all three series show lower Mg# (Mg# 42–68) than the juvenile clinopyroxenes mantling these cores (Mg# 77–72). Thus, these cores must have been incorporated during ascent. The euhedral cores represent melts that were more highly differentiated than any of the magmas

that erupted in the BMVF. As these cores are common in the erupting basanitic magmas, the storage area of these highly differentiated magmas must have been of wide horizontal extent. According to Watanabe et al. (1999), the emplacement of magma storage systems preferentially occurs at density differences in the mantle-crust system, the largest of which is developed at the MOHO. As some of the anhedral clinopyroxene cores are green coloured, with Fe correlating with Na, they can be taken as proof for a high-pressure origin (Duda and Schmincke, 1985). We assume that these cores were incorporated from a magma storage system at the MOHO, which is believed to be located at ~36 km beneath the BMVF (Lucassen et al., 2011).

Clinopyroxenes without xenocrystic cores are titaniferous diopsides, generally with increasing Ca and Ti contents outwards. However, they are oscillatory zoned and exhibit internal resorption textures. Thus, the phenocrysts experienced a convective movement of a continuously cooling and differentiating magma column that underwent magma mixing with less differentiated, hotter magmas. In thin sections, we see proof for these mingling processes by matrices of different crystallinity that must have occurred up to the moment of eruption.

All of these observations characterise samples of all three series, which either occur individually in single eruption centres (CC9, CC44, M3, M5, M6, M8, M11, DX1, DX2 and DX3), or even as magmas of two series in one eruption centre (CC6, CC48, CC53 and M7). Only in one instance, magmas of all three series are represented in the samples of one cinder cone (CC10) (Fig. 1C). The distribution of rocks from Series A-C does not show a systematic pattern. The melts existed at the same time and their conduits must have been interconnected. Thus, the magma plumbing systems of the eruption centres within the BMVF were more complex than expected for a monogenetic volcanic field.

5.3. Isotopic nature of the mantle source

Tightly grouped Sr, Nd, Hf and Pb isotope ratios indicate that the primary melts of the rocks in the BMVF formed from a uniform mantle source (Fig. 10). The presentation of the $^{87}Sr/^{86}Sr$ vs. $^{206}Pb/^{204}Pb$ data shows that there is no indication for the involvement of the mantle endmembers DMM, EM1 and EM2 in the mantle source of the BMVF melts (Fig. 10B). Instead, the samples rather lie on a strict mixing line between the FOZO reference field and the HIMU endmember. Therefore, they are comparable to the mantle source of the Siebengebirge, which is given as a representative example of the German Cenozoic intraplate volcanic fields (Kolb et al., 2012). This characterisation as HIMU-OIB type source supports the classification based on the incompatible trace element distribution (Fig. 9, Fig. 12), which indicates the presence of garnet and at least one hydrous phase in the lherzolitic source. This hydrous phase is suggested by the K vs. La variation to be amphibole. It is assumed that the HIMU component is contained in this hydrous phase of a lithospheric mantle as a consequence of metasomatism (Ball et al., 2019; Geldmacher et al., 2011; Janney et al., 2002; Rooney et al., 2014; Scott et al., 2016; Späth et al., 2001; Sprung et al., 2007).

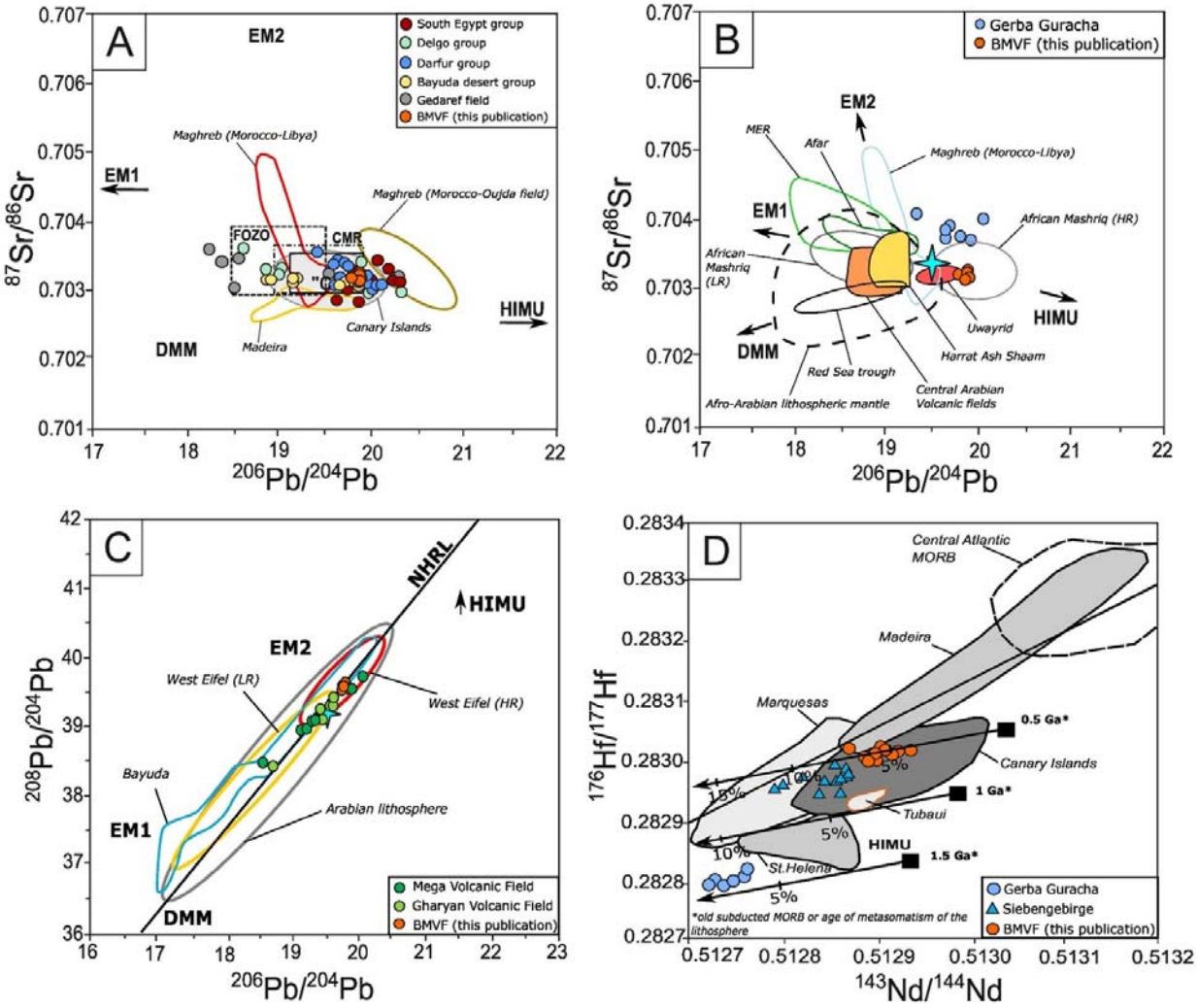

Fig. 15. $^{206}Pb/^{204}Pb$ vs. $^{87}Sr/^{86}Sr$ diagram comparing the isotope ratios of the BMVF to the African Mashriq volcanic provinces (South Egypt group, Delgo group, Darfur group and the Bayuda Desert group) and Gedaref Volcanic Field (Lucassen et al., 2008). In addition, the reference fields of the Canary Islands and Madeira Island (http://georoc.mpch-mainz.gwdg.de/georoc), the Maghrebian (Morocco-Libya) and (Morocco-Oujda) volcanic provinces (Bardintzeff et al., 2012; Duggen et al., 2005) are also plotted. B) $^{206}Pb/^{204}Pb$ vs. $^{87}Sr/^{86}Sr$, the BMVF compared to the Gerba Guracha (Rooney et al., 2014) and the Uwayrid volcanic fields (Altherr et al., 2019) in addition to the refence fields of the Maghreb (Morocco-Libya) and African Mashriq (high radiogenic and low radiogenic group, see text.); MER and Afar volcanic fields (Ayalew et al., 2016), Jordan Volcanic Rocks, Central Arabian volcanic fields, and the Red Sea Trough (Altherr et al., 2019, and references therein). C) Isotopic ratios of the BMVF compared to the Gharyan Volcanic Field (Beccaluva et al., 2008) and the Mega Volcanic Field (Bianchini et al., 2014) alongside the mantle xenolith reference fields of the Arabian lithosphere (Shaw et al., 2007), Bayuda Desert (Lucassen et al., 2011) and the high and low radiogenic xenoliths of the Eifel Volcanic Field in Germany (Witt-Eickschen et al., 2003). D) $^{176}Hf/^{177}Hf$ vs. $^{143}Nd/^{144}Nd$ diagram, highlighting the age and % of sediment input of the metasomatism of the BMVF, Gerba Guracha (reference same as above) and Siebengebirge (references same as in Fig. 10) mantle sources.

In order to understand the relevance of the isotopic ratios of the BMVF in the regional framework of the North Africa section of the circum-Mediterranean volcanic provinces, we compare them with those of volcanic rocks from islands in the Eastern North Atlantic (Madeira and Canary Islands), as well as the Maghrebian volcanic provinces (in Morocco and

Libya) and the African Mashriq volcanic fields (Sudan and Egypt) in Fig. 15A. A compilation of data for the volcanic fields in Sudan and Southern Egypt was published by Lucassen et al. (2008). They are characterised by uniform $^{87}Sr/^{86}Sr$ ratios of 0.703000–0.703800 while $^{206}Pb/^{204}Pb$ ratios spread from 18.200–20.300, however, forming two groups of low and high $^{206}Pb/^{204}Pb$ ratios, respectively, with respect to the $^{206}Pb/^{204}Pb$ value of 19.500 for "C", the common mantle reservoir as defined by Hanan and Graham (1996) (Fig. 15A). The new data plot within the group of high $^{206}Pb/^{204}Pb$ ratios (>19.500), which is mainly defined by the lavas of the Darfur group. Compared to the FOZO reference field, this group of analyses lies outside of the FOZO on the mixing line with the HIMU endmember, partly within the high $^{206}Pb/^{204}Pb$ (i.e. more radiogenic) half of the "C" and Common Mantle Reservoir (CMR) reference fields. As reference field "C" is more strictly defined ($^{206}Pb/^{204}Pb$ 19.500 ±0.3, $^{87}Sr/^{86}Sr$ 0.703300 ±0.000300) relative to both, FOZO and CMR, we also use "C" as a reference field in further figures. In order to increase its visibility, the "C" is represented by a single point (the star in Fig. 15b) with the average ratios of $^{87}Sr/^{86}Sr$ of 0.703300 and $^{206}Pb/^{204}Pb$ of 19.500.

The comparison with data for the E-Atlantic islands and the Maghreb shows that the data for Madeira are similar in $^{206}Pb/^{204}Pb$ to the range of CMR values, being lower in $^{87}Sr/^{86}Sr$ ratios. The $^{206}Pb/^{204}Pb$ data show an extension on the low radiogenic Pb side (<19.500) towards the DMM endmember. The Canary magmas exhibit the same wide range in $^{87}Sr/^{86}Sr$ ratios as the Mashriq, but show a lower range in $^{206}Pb/^{204}Pb$ ratios from 18.180–20.200, centring around "C". Almost all $^{206}Pb/^{204}Pb$ ratios for the Maghrebian volcanic fields plot on the low radiogenic side of "C", with a higher variation in $^{87}Sr/^{86}Sr$. Only the Maghrebian volcanic field of Oujda in Morocco exhibits a high radiogenic $^{206}Pb/^{204}Pb$ character, similar to the volcanic fields of the Mashriq. This indicates that apart from the Ahaggar (Allègre et al., 1981; not shown here) only the magmas in the Oujda field exhibit a HIMU-OIB character within the Maghreb.

For further comparison of the Mashriq data with volcanic fields within the Arabian plate and the Afar/Mid-Ethiopian Rift (MER) region, we turn the data points of the Mashriq volcanic fields into reference fields and only keep the data of the Maghreb as representing the low radiogenic volcanic fields in North Africa (Fig. 15B). The Central Arabian fields and the Harrat Ash Shaam field of Jordan exhibit the same $^{87}Sr/^{86}Sr$ ratios as the Mashriq fields but, similar to the Maghrebian volcanic fields, plot on the lower radiogenic side of "C", exhibiting $^{206}Pb/^{204}Pb$ ratios of 18.600–19.300; also on the Arabian plate, only one volcanic field, Uwayrid, exhibits a high radiogenic HIMU-OIB character within the "C" field.

Compared with the Afar region, the $^{206}Pb/^{204}Pb$ ratios of the Main Ethiopian Rift (MER) exhibit a low radiogenic Pb character, exhibiting ratios of less than 19.300. Additionally, the MER ratios are displaced to lower $^{206}Pb/^{204}Pb$ ratios when compared to the Afar. In both regions, decreasing $^{206}Pb/^{204}Pb$ ratios correlate with increasing $^{87}Sr/^{86}Sr$ ratios. Furthermore, in the MER only one volcanic field, Gerba Guracha, exhibits a high radiogenic HIMU-OIB type character but with higher $^{87}Sr/^{86}Sr$ ratios than the rocks from the Arabian Uwayrid field. The $^{87}Sr/^{86}Sr$ and $^{206}Pb/^{204}Pb$ ratios of spinel-lherzolitic mantle xenoliths within rocks from Afro-Arabian volcanic fields, as given in Fig. 13 of (Ayalew et al., 2018), were used as comparison fields to represent the Afro-Arabian mantle in Fig. 15B. Their variation is of low radiogenic $^{206}Pb/^{204}Pb$ character and complements that of the lavas from the Red Sea Trough, the Arabian volcanic fields, the Harrat Ash Shaam, the Afar and most of the MER.

In the next step, a comparison of the BMVF data with available spinel lherzolitic mantle xenoliths is intended. However, while $^{87}Sr/^{86}Sr$ ratios are not given for all xenoliths, $^{208}Pb/^{204}Pb$ ratios are more readily available. Therefore, we base the comparison on $^{208}Pb/^{204}Pb$ in relation to $^{206}Pb/^{204}$ Pb ratios (Fig. 15C). By comparing the lavas with spinel-lherzolitic xenoliths from the shallow mantle, we do not imply that the lavas are generated at these shallow levels. We are aware that these xenoliths are only broken fragments of the rigid lithospheric mantle brought up by rising magmas that were generated in the garnet-lherzolite mantle. For comparison, we selected the Pb isotope ratios of xenoliths from (a) the Bayuda Desert fields (Lucassen et al., 2008), (b) the Harrat Ash Shaam field, addressed as being representative for the Arabian lithosphere (Shaw et al., 2007), (c) the West Eifel Volcanic Field in Germany (LR = amphibole free, HR = amphibole-bearing) (Witt-Eickschen et al., 2003), as well as data points for analyses from (d) the Mega Volcanic Field in the southern MER (Bianchini et al., 2014), and (e) the Gharyan Volcanic Field in northern Libya, Maghreb (Beccaluva et al., 2008). The majority of the xenoliths show low radiogenic Pb character. Only a minority (including the Mega and Gharyan volcanic fields) shows high radiogenic Pb character and complement the composition of the amphibole-bearing xenoliths of the West Eifel Volcanic Field.

To test the age of the high radiogenic Pb information in the mantle source of the BMVF, we used a model developed by Geldmacher et al. (2011) for the Canary Islands that is based on Hf/Nd isotope characteristics (Fig. 15D). In their model, the authors assumed that the mantle character that causes the isotopic composition in the volcanic rocks to deviate from the common mantle source is introduced as a subducted oceanic crust component which is overlain by recycled continental sediments. While the age of the introduction dominantly determines the $^{176}Hf/^{177}Hf$ ratios, the amount of incorporated continental sediments determines the $^{143}Nd/^{144}Nd$ ratios. Transferring this model to the BMVF, following Geldmacher et al. (2011), we interpret the $^{176}Hf/^{177}Hf$ ratios as indicating the age of the metasomatic overprint of the sub-continental lithosphere of the BMVF by fluids from dehydration of subducting ocean crust and overlying sediments. The $^{176}Hf/^{177}Hf$ – $^{143}Nd/^{144}Nd$ characteristics of the BMVF samples indicate an age for the HIMU-type metasomatism of ~0.55 Ga. For comparison, an age of metasomatism of ca. 1.3-1,2 Ga is indicated for the mantle source of the lavas of the Gerba Guracha field in the eastern MER. An age of 0.8-0.55 Ga is given for the metasomatism of the mantle source of the Siebengebirge rocks in Germany. The age of ~0.55 Ga, given for the metasomatic event of the BMVF mantle source, coincides with the age of the younger orogeny within the Pan-African event, the Kuunga orogeny, for which an age of 0.55 Ga is given (Meert and Van Der Voo, 1997). This age is only in minor contradiction to Barth and Meinhold (1979) who dated the metasomatism of the complete series of the Precambrian basement complex in the Bayuda area to 725-600 Ma.

Our data show that the high radiogenic Pb isotope characteristics of the BMVF of $^{206}Pb/^{204}Pb$ ratios of >19.500 match those of the NE African part of the Mashriq in the Sudan and S-Egypt. Only individual volcanic fields within the Maghreb (Oujda, Ahaggar), the Arabian plate (Uwayridd) and the Afar/MER region (Gerba Guracha) exhibit the same HIMU-OIB-type composition.

This leads to a variety of different interpretations: Allègre et al. (1981) and Franz et al. (1994) interpret the Darfur Dome and its related volcanism (Jebel Marra, Tabago Hills and Meidob

Hills) to be the product of a weak asthenospheric diapir. Duggen et al. (2005) believe the lavas of the Maghrebian margin to be the product of delamination of the subcontinental lithosphere, causing passive upwelling of the asthenosphere, containing the CMR signature (Cebrià and Wilson, 1995). Hanan and Graham (1996) argue that the HIMU-signature is brought up to the surface by mantle plumes of common mantle composition "C" that arise from the core-mantle boundary and incorporate this and all other mantle endmember signatures during ascent. Chauvel et al. (1992) also argue that the HIMU-signature is contained in mantle plumes but is already part of the rising plume from the start. In contrast, Janney et al. (2002) argue that a common source with a HIMU-signature is too prevalent throughout NE, E and S Africa to be ascribed as chemical signature of numerous individual mantle plumes causing the volcanism. They continue to argue that the signature must be a characteristic of either the African lithosphere or the convecting asthenospheric mantle (Janney et al., 2002).

As a hydrous phase such as amphibole, which is required in the mantle source of the melts within melting models, is not stable in the convecting asthenospheric mantle or thermally anomalous plumes (Class and Goldstein, 1997, Wallace and Green, 1991), a lithospheric mantle source is favoured (Ball et al., 2019, Lucassen et al., 2008, Lustrino and Wilson, 2007, Nelson et al., 2019, Rooney et al., 2014, Scott et al., 2016, Späth et al., 2001, Stein and Hofmann, 1992). However, a HIMU-signature in the lithospheric mantle cannot be derived from direct metasomatism by young supra-subduction fluids as those could only explain the opposite low radiogenic $^{206}Pb/^{204}Pb$ character. This, as well as uniform isotopic melt characteristics in several volcanic fields of different ages in a region such as the Maghreb, Mashriq or Arabian subplate, lead several authors to propose a model in which young high-temperature anomalies in the asthenospheric mantle resulted in tapping the overlying metasomatised mantle that gained its EM- or HIMU-signature from a contribution of a fossil mantle plume to the lithosphere (Stein and Hofmann, 1992; Wilson et al., 2000; Sprung et al., 2007). The final derivation of the BMVF melts from a metasomatised lithospheric mantle source is thought to be necessary as a hydrous phase such as amphibole is indicated in melting models that are based on incompatible element data. However, it cannot be concluded that the presence of amphibole in the source directly implies a HIMU-signature in the resulting melts. This is indicated by the correlation diagram of K versus La (Fig. 14A), which shows that melts with low radiogenic $^{206}Pb/^{204}Pb$ character like those in the Afar/MER also exhibit a low K character.

As a melting model, we suggest that the BMVF magmas were generated by the tapping of a metasomatised amphibole peridotitic lithospheric mantle, bearing a HIMU-signature through a Quaternary thermal anomaly in the asthenospheric mantle, as indicated by an upwarped lithosphere-asthenosphere boundary (LAB) in Ball et al. (2019). King and Ritsema (2000) suggest edge-driven convection in the upper mantle, controlled by thick cratonic lithosphere, as the source for the rise of small scale temperature anomalies to explain the location of volcanic fields within the African plate. When applying the model of Geldmacher et al. (2011), which is based on Hf/Nd isotope variations, the age of 0.55 Ga for the HIMU-signature within the mantle source of the BMVF is interpreted as the age of metasomatism of the lithospheric mantle.

This model is completely independent of the principle genesis of the HIMU-signature in the convecting mantle: the most accepted model suggests inherited altered oceanic crust (AOC) losing Pb during the decomposition of hydrous silicate phases during subduction into the lower mantle more than 2.0 Ga ago (Chauvel et al., 1992; Hanan and Graham, 1996; Hanyu et al., 2011), a model which is also supported by He, Ne and S isotopes (Cabral et al., 2013; Parai et al., 2009). Recently, it was pointed out that the volatile characteristics of the HIMU-like signature require additional subduction of carbonate, whether in form of marine carbonates (Castillo, 2015) or serpentinised peridotite (Pettke et al., 2018), independent of the depth of storage in the lower mantle or the transition zone of the upper mantle (Mazza et al., 2019). Weiss et al. (2016) propose an alternative model in which an Archean to early Proterozoic subcontinental lithospheric mantle that was previously metasomatised by fluids/melts with carbonatitic affinity from subducting slabs is subsequently incorporated into the convecting mantle by delamination.

6. Conclusions

The new petrographic and geochemical results of this contribution allow the following constraints:

- The analysed volcanic rocks from the BMVF are of basanitic to hawaiitic composition, characterising it as a sodic-alkaline volcanic field. Based on major and minor element variations, combined with petrographic and minerochemical evidence, the magmas experienced fractionation of prodominantly olivine and clinopyroxene, the main phenocryst phases, that were accompanied by early spinel of the chromite series and late spinel of the magnetite series as well as apatite. Except for apatite, all fractionated phases were identified as solidus phases in thin sections. Petrographic evidence documents that the FC processes were accompanied by assimilation of mantle and crustal rocks as well as mingling and mixing processes until shortly before to their eruption.
- •Based on systematic differences in trace element variations, two primary magma series, Series A and B, can be distinguished. A third magma series, Series C, can be distinguished as well, exhibiting distinctive trace element variations, enrichment of Sc, REE and the LILE elements, but whose genesis is not entirely understood. A derivation from Series A by mixing with a specific co-magmatic component is postulated.
- •Based on uniform normalised incompatible element patterns, e.g. LREE enrichment accompanied by HREE depletion, and negative depletions of K and Pb, all magmas are of OIB-type and require the presence of garnet in the mantle source. This suggests that the melts formed at depths within the garnet stability zone (2.0–2.2 GPa at 1200–1300°C). Pronounced K-depletions indicate a hydrous amphibole-bearing source lithology for the BMVF melts. Yb/La and Dy/La modelling estimates that Series A and B formed from an amphibole-garnet lherzolitic source through 5–6% and 4% partial melting, respectively. The presence of amphibole provides a constraint, implying that the melt was derived from a metasomatised lithospheric mantle.
- •The presence of the Pb-depletion (documented by Ce/Pb ratios of >30) suggests that all magmas are of HIMU-OIB type. This is supported by their uniform Sr, Nd, Hf and Pb isotope characteristics, by which their source mantle is characterised by the composition of the common mantle “C” with an overprint by a HIMU component,

resulting in higher radiogenic $^{206}Pb/^{204}Pb$ ratios above 19.5 (FOZO-HIMU-OIB type). Hf/Nd isotopes suggest that this HIMU information was introduced into the lithospheric mantle below the BMVF at ca. 0.55 Ga.

- •The BMVF source is comparable to that of the majority of volcanic fields in Sudan and southern Egypt as the more radiogenic group within the common isotopic mantle reservoir (CMR) of the alkaline mafic volcanics in anorogenic fields in the Circum-Mediterranean Cenozoic Igneous Province, including the Cenozoic European and North African volcanic fields.
- •In contrast to most samples from the volcanic fields in the Maghreb, the Arabian plate as well as the Afar/MER region the BMVF samples do not show any indication of an input from another endmember, e.g. EM or DMM. A slight offset of only one sample towards the upper crustal endmember is due to the assimilation of crustal rocks as indicated by xenoliths of the Bayuda basement.
- •The high radiogenic Pb character of the BMVF indicates that its genesis cannot be related to magmatism associated with the activity of the Afar plume event and associated magmatism along the MER and the Red Sea Rift, as they all are of low radiogenic character with an additional asthenospheric overprint in the case of the Red Sea Rift magmas.
- •In all of northern Africa (including Ethiopia) and Arabia only single volcanic fields, e.g. the Oujda and the Ahaggar in the Maghreb, the Uwayrid on the Arabian subplate and Gerba Guracha in the Afar/Ethiopia region share the high radiogenic (HIMU-OIB) character of the Sudan-South Egypt fields. As this characteristic is attributed to metasomatism of the lithospheric mantle, the data indicate that the HIMU-signature is more pervasive in the Sudan while being locally restricted in the Maghreb, the African subplate as well as the MER region.

Declaration of Competing Interest

The authors declare that they have no known competing financial interests or personal relationships that could have appeared to influence the work reported in this paper.

The authors declare the following financial interests/personal relationships which may be considered as potential competing interests.

Acknowledgments

N.L. thanks the National Research Foundation of South Africa (NRF) for financial support (Grant number 127060). Christian Reinke from the University of Johannesburg is thanked for his help during microprobe analysis. We thank editor Greg Shellnutt, and Paul Béguelin and an anonymous reviewer for their valuable reviews. Their suggestions have significantly improved the quality of the paper.

References

Abdelsalam, M.G., Abdel-Rahman, E.-S.M., El-Faki, E.-F.M., Al-Hur, B., El-Bashier, F.-R. M., Stern, R.J., Thurmond, A.K., 2003. Neoproterozoic deformation in the northeastern part of the Saharan Metacraton, northern Sudan. Precambrian Res. 123, 203–221.

Adam, J., Green, T., 2006. Trace element partitioning between mica-and amphibole-bearing garnet lherzolite and hydrous basanitic melt: 1. Experimental results and the investigation of controls on partitioning behaviour. Contrib. Mineral. Petrol. 152 (1), 1–17.

Allègre, C.J., Dupré, B., Lambret, B., Richard, P., 1981. The subcontinental versus suboceanic debate, I Lead-neodymium-strontium isotopes in primary alkali basalts from a shield area the Ahaggar volcanic suite. Earth Planet. Sci. Lett. 52 (1), 85–92.

Almond, D.C., 1974. The composition of basaltic lavas from Bayuda, Sudan and their place in the cainozoic volcanic history of north-East Africa. Bull. Volcanol. 38, 345–360.

Almond, D.C., Ahmed, F., Khalil, B.E., 1969. An excursion to the Bayuda volcanic field of Northern Sudan. Bull. Volcanol. 33, 549–565.

Almond, D.C., Kheir, O.M., Poole, S., 1984. Alkaline basalt volcanism in northeastern Sudan: a comparison of the Bayuda and Gedaref areas. J. Afr. Earth Sci. 2, 233–245.

Altherr, R., Mertz-Kraus, R., Volker, F., Kreuzer, H., Henjes-Kunst, F., Lange, U., 2019. Geodynamic setting of Upper Miocene to Quaternary alkaline basalts from Harrat al 'Uwayrid (NW Saudi Arabia): Constraints from KAr dating, chemical and Sr-Nd-Pb isotope compositions, and petrological modeling. Lithos 330, 120–138.

Ayalew, D., Jung, S., Romer, R.L., Garbe-Schönberg, D., et al., 2018. Trace element systematics and Nd, Sr and Pb isotopes of Pliocene flood basalt magmas (Ethiopian rift): a case for Afar plume-lithosphere interaction. Chem. Geol. 493, 172–188.

Ayalew, D., Jung, S., Romer, R.L., Kersten, F., Pfänder, J.A., Garbe-Schönberg, D., 2016. Petrogenesis and origin of modern Ethiopian rift basalts: Constraints from isotope and trace element geochemistry. Lithos 258, 1–14.

Ball, P.W., White, N.J., Masoud, A., Nixon, S., Hoggard, M.J., Maclennan, J., Stuart, F.M., Oppenheimer, C., Kröpelin, S., 2019. Quantifying asthenospheric and lithospheric controls on mafic magmatism across North Africa. Geochem. Geophys. Geosyst. 20 (7), 3520–3555.

Bardintzeff, J.M., Deniel, C., Guillou, H., Platevoet, B., Télouk, P., Oun, K.M., 2012. Miocene to recent alkaline volcanism between Al Haruj and Waw an Namous (southern Libya). Int. J. Earth Sci. 101 (4), 1047–1063.

Barth, H., Meinhold, K.D., 1979. Mineral Prospecting in the Bayuda Desert. Bundesanstalt für Geowissenschaften und Rohstoffe, Hannover, Germany, p. 336.

Beccaluva, L., Bianchini, G., Ellam, R.M., Marzola, M., Oun, K.M., Siena, F., Stuart, F.M., et al., 2008. The role of HIMU metasomatic components in the North African lithospheric mantle: petrological evidence from the Gharyan lherzolite xenoliths, NW Libya. Geolog. Soc. London Spec. Publ. 293 (1), 253–277.

Bianchini, G., Bryce, J.G., Blichert-Toft, J., Beccaluva, L., Natali, C., et al., 2014. Mantle dynamics and secular variations beneath the East African Rift: insights from peridotite xenoliths (Mega, Ethiopia). Chem. Geol. 49–58.

Bizimis, M., Salters, V.J., Dawson, J.B., 2003. The brevity of carbonatite sources in the mantle: evidence from Hf isotopes. Contrib. Mineral. Petrol. 145 (3), 281–300.

Blichert-Toft, J., Chauvel, C., Albarède, F., 1997. Separation of Hf and Lu for high-precision isotope analysis of rock samples by magnetic sector-multiple collector ICP-MS. Contrib. to Mineral. Petrol. 127 (3), 248–260.

Bouvier, A., Vervoort, J.D., Patchett, P.J., 2008. The Lu–Hf and Sm–Nd isotopic composition of CHUR: constraints from unequilibrated chondrites and implications for the bulk composition of terrestrial planets. Earth Planet. Sci. Lett. 273 (1–2), 48–57.

Brenna, M., Cronin, S.J., Nemeth, K., Smith, I.E., Sohn, Y.K., 2011. The influence of magma plumbing complexity on monogenetic eruptions, Jeju Island, Korea. Terra Nova 23, 70–75.

Cabral, R.A., Jackson, M.G., Rose-Koga, E.F., Koga, K.T., Whitehouse, M.J., Antonelli, M.A., Farquhar, J., Day, J.M., Hauri, E.H., 2013. Anomalous Sulphur isotopes in plume lavas reveal deep mantle storage of Archaean crust. Nature 496 (7446), 490–493.

Castillo, P.R., 2015. The recycling of marine carbonates and sources of HIMU and FOZO Ocean island basalts. Lithos 216, 254–263.

Cebrià, J.M., Wilson, M., 1995. Cenozoic mafic magmatism in Western/Central Europe: a common European asthenospheric reservoir? Terra Nova Abstract Suppl, EGU 7, 162.

Chauvel, C., Hofmann, A.W., Vidal, P., 1992. HIMU-EM: the French Polynesian connection. Earth Planet. Sci. Lett. 110 (1–4), 99–119.

Class, C., Goldstein, S.L., 1997. Plume-lithosphere interactions in the ocean basins: constraints from the source mineralogy. Earth Planet. Sci. Lett. 150 (3–4), 245–260.

Coote, A., Shane, P., Fu, B., 2019. Olivine phenocryst origins and mantle magma sources for monogenetic basalt volcanoes in northern New Zealand from textural, geochemical and δ18O isotope data. Lithos 344, 232–246.

Dawson, J.B., 2008. The Gregory Rift Valley and Neogene- Recent Volcanoes of Northern Tanzania. Geological Society Memoir 33. Geological Society, London, p. 102.

Duda, A., Schmincke, H.U., 1985. Polybaric differentiation of alkali basaltic magmas: evidence from green-core clinopyroxenes (Eifel, FRG). Contrib. Mineral. Petrol. 91 (4), 340–353.

Duggen, S., Hoernle, K., van den Bogaard, P., Garbe-Schönberg, D., 2005. Post-collisional transition from subduction-to intraplate-type magmatism in the western most Mediterranean: evidence for continental-edge delamination of subcontinental lithosphere. J. Petrol. 46 (6), 1155–1201.

Franz, G., Pudlo, D., Urlacher, G., Haussmann, U., Boven, A., Wemmer, K., 1994. The Darfur Dome, western Sudan: the product of a subcontinental mantle plume. Geologische Rundschau 83 (3), 614–623.

Galer, S.J.G., Abouchami, W., 1998. Practical application of lead triple spiking for correction of instrumental mass discrimination. Mineral. Mag. 62, 491–492.

Geldmacher, J., Hoernle, K., Hanan, B.B., Blichert-Toft, J., Hauff, F., Gill, J.B., Schmincke, H.U., 2011. Hafnium isotopic variations in East Atlantic intraplate volcanism. Contrib. Mineral. Petrol. 162 (1), 21–36.

Govindaraju, K., 1994. 1994 compilation of working values and sample description for 383 geostandards. Geostand. Newslett. 18, 1–158.

Green, D.H., Falloon, T.J., 1998. Pyrolite: A ringwood concept and its current expression. In: Jackson, I. (Ed.), The Earth's Mantle: Composition, Structure, and Evolution. Cambridge University Press, Cambridge, pp. 311–378.

Green, D.H., Edgar, A.D., Beasley, P., Kiss, E., Ware, N.G., 1974. Upper mantle source for some hawaiites, mugearites and benmoreites. Contrib. Mineral. Petrol. 48 (1), 33–43.

Hanan, B.B., Graham, D.W., 1996. Lead and helium isotope evidence from oceanic basalts for a common deep source of mantle plumes. Science 272 (5264), 991–995.

Hanyu, T., Tatsumi, Y., Senda, R., Miyazaki, T., Chang, Q., Hirahara, Y., Takahashi, T., Kawabata, H., Suzuki, K., Kimura, J.I., Nakai, S.I., 2011. Geochemical characteristics and origin of the HIMU reservoir: a possible mantle plume source in the lower mantle. Geochem. Geophys. Geosyst. 12 (2).

Harris, C., Dreyer, T., Le Roux, P., 2018. Petrogenesis of peralkaline granite dykes of the Straumsvola complex, western Dronning Maud Land, Antarctica. Contrib. Mineral. Petrol. 173 (1), 8.

Hart, S.R., 1984. A large-scale isotope anomaly in the Southern Hemisphere mantle. Nature 309 (5971), 753–757.

Hartmann, G., Wedepohl, K.H., 1990. Metasomatically altered peridotite xenoliths from the Hessian Depression (Northwest Germany). Geochim. Cosmochim. Acta 54 (1), 71–86.

Hauri, E.H., Whitehead, J.A., Hart, S.R., 1994. Fluid dynamic and geochemical aspects of entrainment in mantle plumes. J. Geophys. Res. Solid Earth 99 (B12), 24275–24300.

Hofmann, A.W., 2003. Sampling mantle heterogeneity through oceanic basalts: isotopes and trace elements. Treat. Geochem. 2, 61–101.

Irvine, T.N., Baragar, W.R.A., 1971. A guide to the chemical classification of the common volcanic rocks. Canad. J. Earth Sci. 8 (5), 523–548.

Janney, P.E., Le Roex, A.P., Carlson, R.W., Viljoen, K.S., 2002. A chemical and multi-isotope study of the Western Cape olivine melilitite province, South Africa: implications for the sources of kimberlites and the origin of the HIMU signature in Africa. J. Petrol. 43 (12), 2339–2370.

Kereszturi, G., Geyer, A., Martí, J., Németh, K., Dóniz-Páez, F.J., 2013. Evaluation of morphometry-based dating of monogenetic volcanoes—a case study from Bandas del Sur, Tenerife (Canary Islands). Bull. Volcanol. 75 (7), 1–19.

King, S.D., Ritsema, J., 2000. African hot spot volcanism: small-scale convection in the upper mantle beneath cratons. Science 290 (5494), 1137–1140.

Kirchenbaur, M., Münker, C., Schuth, S., Garbe-Schönberg, D., Marchev, P., 2012. Tectonomagmatic constraints on the sources of Eastern Mediterranean K-rich lavas. J. Petrol. 53 (1), 27–65.

Kolb, M., Paulick, H., Kirchenbaur, M., Münker, C., 2012. Petrogenesis of mafic to felsic lavas from the Oligocene Siebengebirge volcanic field (Germany): implications for the origin of intracontinental volcanism in Central Europe. J. Petrol. 53 (11), 2349–2379.

LaTourrette, T., Hervig, R.L., Holloway, J.R., 1995. Trace element partitioning between amphibole, phlogopite, and basanite melt. Earth Planet. Sci. Lett. 135, 13–30.

Le Maitre, R.W., Streckeisen, A., Zanettin, B., Le Bas, M.J., Bonin, B., Bateman, P., Bellieni, G., Dudek, A., Efremova, S., Keller, J., Lameyre, J., Sabine, P.A., Schmid, R., Srensen, H., Woolley, A.R., 2002. Recommendations of the International Union of Geological Sciences Subcommission on the Systematics of Igneous Rocks. Igneous Rocks: A Classification and Glossary of Terms, 2nd. Cambridge University Press.

Lenhardt, N., Borah, S.B., Lenhardt, S.Z., Bumby, A.J., Ibinoof, M.A., Salih, S.A., 2018. The monogenetic Bayuda Volcanic Field, Sudan – New insights into geology and volcanic morphology. J. Volcanol. Geotherm. Res. 356, 211–224.

Liégeois, J.P., Benhallou, A., Azzouni-Sekkal, A., Yahiaoui, R., Bonin, B., 2005. The Hoggar swell and volcanism: reactivation of the Precambrian Tuareg shield during Alpine convergence and West African Cenozoic volcanism. In: Foulger, G.R., Natland, J.H., Presnall, D.C., Anderson, D.L. (Eds.), Plates, Plumes and Paradigms: Geological Society of America Special Paper 388, 379–400002E.

Liégeois, J.P., Abdelsalam, M.G., Ennih, N., Ouabadi, A., 2013. Metacraton: nature, genesis and behavior. Gondwana Res. 23 (1), 220–237.

Lucassen, F., Franz, G., Romer, R.L., Pudlo, D., Dulski, P., 2008. Nd, Pb, and Sr isotope composition of late Mesozoic to Quaternary intra-plate magmatism in NE-Africa (Sudan, Egypt): high-μ signatures from the mantle lithosphere. Contrib. Mineral. Petrol. 156 (6), 765–784.

Lucassen, F., Franz, G., Romer, R.L., Dulski, P., 2011. Late Mesozoic to Quaternary intraplate magmatism and its relation to the Neoproterozoic lithosphere in NE Africa—New data from lower-crustal and mantle xenoliths from the Bayuda volcanic field, Sudan. In: Beccaluva, L., Bianchini, G., Wilson, M. (Eds.), Volcanism and Evolution of the African Lithosphere. Geological Society of America Special Paper 478, pp. 1–24.

Lustrino, M., Wilson, M., 2007. The circum-Mediterranean anorogenic Cenozoic igneous province. Earth Sci. Rev. 81 (1–2), 1–65.

Mazza, S.E., Gazel, E., Bizimis, M., Moucha, R., Béguelin, P., Johnson, E.A., McAleer, R.J., Sobolev, A.V., 2019. Sampling the volatile-rich transition zone beneath Bermuda. Nature 569 (7756), 398–403.

McDonough, W.F., Sun, S.S., 1995. The composition of the Earth. Chem. Geol. 120 (3–4), 223–253.

Meert, J.G., Van Der Voo, R., 1997. The assembly of Gondwana 800-550 Ma. J. Geodyn. 23 (3–4), 223–235.

Münker, C., Weyer, S., Scherer, E., Mezger, K., 2001. Separation of high field strength elements (Nb, Ta, Zr, Hf) and Lu from rock samples for MC-ICPMS measurements. Geochem. Geophys. Geosyst. 2 https://doi.org/10.1029/2001GC000183.

Nelson, W.R., Hanan, B.B., Graham, D.W., Shirey, S.B., Yirgu, G., Ayalew, D., Furman, T., 2019. Distinguishing plume and metasomatized lithospheric mantle contributions to post-flood basalt volcanism on the south eastern Ethiopian Plateau. J. Petrol. 60 (5), 1063–1094.

Németh, K., 2010. Monogenetic volcanic fields: origin, sedimentary record, and relationship with polygenetic volcanism. Geol. Soc. Am. Spec. Pap. 470, 43–66.

Németh, K., Kereszturi, G., 2015. Monogenetic volcanism: personal views and discussion. Int. J. Earth Sci. 104, 2131–2146.

Németh, K., White, J.D., Reay, A., Martin, U., 2003. Compositional variation during monogenetic volcano growth and its implications for magma supply to continental volcanic fields. J. Geol. Soc. 160, 523–530.

Nesbitt, H., Young, G.M., 1982. Early Proterozoic climates and plate motions inferred from major element chemistry of lutites. Nature 299 (5885), 715–717.

Ngwa, C.N., Lenhardt, N., Le Roux, P., Mbassa, B.J., 2019. The Mount Cameroon southwest flank eruptions: Geochemical constraints on the subsurface magma plumbing system. J. Volcanol. Geotherm. Res. 384, 179–188.

Nkouathio, D.G., Ménard, J.J., Wandji, P., Bardintzeff, J.M., 2002. The Tombel graben (West Cameroon): a recent monogenetic volcanic field of the Cameroon Line. J. Afr. Earth Sci. 35, 285–300.

O'Hara, M.J., Richardson, S.W., Wilson, G., 1971. Garnet-peridotite stability and occurrence in crust and mantle. Contrib. Mineral. Petrol. 32 (1), 48–68.

Parai, R., Mukhopadhyay, S., Lassiter, J.C., 2009. New constraints on the HIMU mantle from neon and helium isotopic compositions of basalts from the Cook–Austral Islands. Earth Planet. Sci. Lett. 277 (1–2), 253–261.

Pettke, T., Kodolányi, J., Kamber, B.S., 2018. From ocean to mantle: new evidence for U-cycling with implications for the HIMU source and the secular Pb isotope evolution of Earth's mantle. Lithos 316, 66–76.

Pin, C., Zalduegui, J.S., 1997. Sequential separation of light rare-earth elements, thorium and uranium by miniaturized extraction chromatography: application to isotopic analyses of silicate rocks. Analyt. Chim. Acta 339 (1–2), 79–89.

Roeder, P., Emslie, R., 1970. Olivine-liquid equilibrium. Contrib. Mineral. Petrol. 29, 275–289.

Rooney, T.O., Nelson, W.R., Dosso, L., Furman, T., Hanan, B., 2014. The role of continental lithosphere metasomes in the production of HIMU-like magmatism on the northeast African and Arabian plates. Geology 42 (5), 419–422.

Salters, V.J.M., Stracke, A., 2004. Composition of the depleted mantle. Geochem. Geophys. Geosyst. 5, Q05B07 https://doi.org/10.1029/2003GC000597.

Scott, J.M., Brenna, M., Crase, J.A., Waight, T.E., van der Meer, Q.H., Cooper, A.F., Michael Palin, J., Le Roux, P., Münker, C., 2016. Peridotitic lithosphere metasomatized by volatile-bearing melts, and its association with intraplate alkaline HIMU-like magmatism. J. Petrol. 57 (10), 2053–2078.

Shaw, D.M., 1970. Trace element fractionation during anatexis. Geochim. Cosmochim. Acta 34 (2), 237–243.

Shaw, J.E., Baker, J.A., Kent, A.J.R., Ibrahim, K.M., Menzies, M.A., 2007. The geochemistry of the Arabian lithospheric mantle—a source for intraplate volcanism? J. Petrol. 48 (8), 1495–1512.

Späth, A., Le Roex, A.P., Opiyo-Akech, N., 2001. Plume–Lithosphere Interaction and the Origin of Continental Rift-related Alkaline Volcanism—the Chyulu Hills Volcanic Province, Southern Kenya. J. Petrol. 42 (4), 765–787.

Sprung, P., Schuth, S., Münker, C., Hoke, L., 2007. Intraplate volcanism in New Zealand: the role of fossil plume material and variable lithospheric properties. Contrib. Mineral. Petrol. 153 (6), 669–687.

Stein, M., Hofmann, A.W., 1992. Fossil plume head beneath the Arabian lithosphere? Earth Planet. Sci. Lett. 114 (1), 193–209.

Sun, S.-S., McDonough, W.F., 1989. Chemical and isotopic systematics of oceanic basalts: implications for mantle composition and processes. Geol. Soc. Lond., Spec. Publ. 42, 313–345.

Vail, J., 1985. Alkaline ring complexes in Sudan. J. Afr. Earth Sci. 3, 51–59.

Vail, J.R., 1988. Tectonics and evolution of the Proterozoic basement of Northeastern Africa. In: El-Gaby, S., Greiling, R. (Eds.), The Pan-African Belt of Northeast Africa and Abjacent Areas. Vieweg and Sohn, Braunschweig, pp. 195–226.

Vonopartis, L., Nex, P., Kinnaird, J., Robb, L., 2020. Evaluating the changes from endogranitic magmatic to magmatic-hydrothermal mineralization: the Zaaiplaats Tin Granites, Bushveld Igneous complex, South Africa. Minerals 10 (4), 379.

Wallace, M., Green, D.H., 1991. The effect of bulk rock composition on the stability of amphibole in the upper mantle: implications for solidus positions and mantle metasomatism. Mineral. Petrol. 44 (1–2), 1–19.

Watanabe, T., Koyaguchi, T., Seno, T., 1999. Tectonic stress controls on ascent and emplacement of magmas. J. Volcanol. Geotherm. Res. 91, 65–78.

Weiss, Y., Class, C., Goldstein, S.L., Hanyu, T., 2016. Key new pieces of the HIMU puzzle from olivines and diamond inclusions. Nature 537 (7622), 666–670.

Wijbrans, J., Németh, K., Martin, U., Balogh, K., 2007. 40Ar/39Ar geochronology of Neogene phreatomagmatic volcanism in the western Pannonian Basin, Hungary. J. Volcanol. Geotherm. Res. 164 (4), 193–204.

Wilson, M., Shimron, A.E., Rosenbaum, J.M., Preston, J., 2000. Early cretaceous magmatism of Mount Hermon, Northern Israel. Contrib. Mineral. Petrol. 139 (1), 54–67.

Witt-Eickschen, G., Seck, H.A., Mezger, K., Eggins, S.M., Altherr, R., 2003. Lithospheric mantle evolution beneath the Eifel (Germany): constraints from Sr–Nd–Pb isotopes and trace element abundances in spinel peridotite and pyroxenite xenoliths. J. Petrol. 44 (6), 1077–1095.

Zindler, A., Hart, S., 1986. Chemical geodynamics. Annu. Rev. Earth Planet. Sci. 14 (1), 493–571.